

# Relativistic Tidal Disruption and Nuclear Ignition of White Dwarf Stars by Intermediate Mass Black Holes

PETER ANNINOS,<sup>1</sup> P. CHRIS FRAGILE,<sup>2,3</sup> SAMUEL S. OLIVIER,<sup>4</sup> ROBERT HOFFMAN,<sup>1</sup> BHUPENDRA MISHRA,<sup>5,3</sup> AND  
KAREN CAMARDA<sup>6</sup>

<sup>1</sup>*Lawrence Livermore National Laboratory, Livermore, CA 94550, USA*

<sup>2</sup>*Department of Physics and Astronomy, College of Charleston, Charleston, SC 29424, USA*

<sup>3</sup>*Kavli Institute for Theoretical Physics, Santa Barbara, CA, USA*

<sup>4</sup>*Department of Nuclear Engineering, University of California, Berkeley, CA 94720, USA*

<sup>5</sup>*JILA, University of Colorado and National Institute of Standards and Technology, 440 UCB, Boulder, CO 80309-0440, USA*

<sup>6</sup>*Department of Physics and Astronomy, Washburn University, Topeka, KS 66621, USA*

## ABSTRACT

We present results from general relativistic calculations of the tidal disruption of white dwarf stars from near encounters with intermediate mass black holes. We follow the evolution of 0.2 and 0.6 $M_{\odot}$  stars on parabolic trajectories that approach  $10^3 - 10^4 M_{\odot}$  black holes as close as a few Schwarzschild radii at periastris, paying particular attention to the effect tidal disruption has on thermonuclear reactions and the synthesis of intermediate to heavy ion elements. These encounters create diverse thermonuclear environments characteristic of Type I supernovae and capable of producing both intermediate and heavy mass elements in arbitrary ratios, depending on the strength (or proximity) of the interaction. Nuclear ignition is triggered in all of our calculations, even at weak tidal strengths  $\beta \sim 2.6$  and large periastris radius  $R_P \sim 28$  Schwarzschild radii. A strong inverse correlation exists between the mass ratio of calcium to iron group elements and tidal strength, with  $\beta \lesssim 5$  producing predominately calcium-rich debris. At these moderate to weak interactions, nucleosynthesis is not especially efficient, limiting the total mass and outflows of calcium group elements to  $< 15\%$  of available nuclear fuel. Iron group elements however continue to be produced in greater quantity and ratio with increasing tidal strength, peaking at  $\sim 60\%$  mass conversion efficiency in our closest encounter cases. These events generate short bursts of gravitational waves with characteristic frequencies 0.1-0.7 Hz and strain amplitudes  $0.5 \times 10^{-22} - 3.5 \times 10^{-22}$  at 10 Mpc source distance.

*Keywords:* stars:black holes — white dwarfs — black hole physics — hydrodynamics — nuclear reactions, nucleosynthesis, abundances

## 1. INTRODUCTION

Tidal disruptions (TD) of white dwarf (WD) stars by intermediate mass black holes (IMBH) are complex and violent cosmic events capable of generating significant electromagnetic and potentially observable gravitational wave energies. A star passing by a black hole can be disrupted (elongated and torn apart) while also suffering compression when the black hole tidal force exceeds the star's self-gravity. The debris from disrupted stars will either disperse unbound materials into the surrounding medium, or accrete onto the black hole and produce flares and jets that can be observed electromagnetically (Rees 1988; Haas et al. 2012; MacLeod et al. 2016).

Unlike their supermassive counterparts, observational evidence for IMBHs in their likely host environments, dwarf galaxies or globular clusters, is tentative at best (Gerssen et al. 2002, 2003; Gebhardt et al. 2002, 2005; Dong et al. 2007), fueling efforts to identify signatures from IMBHs like those that might come from tidal disruption events (TDE). Supermassive black holes (greater than  $10^5 M_{\odot}$ ), such as are observed at the centers of many large galaxies, are not likely to disrupt a WD substantially before swallowing it entirely. IMBHs, on the other hand, can be effective disruptors, leading to accretion rates up to  $\sim 10^4 M_{\odot} \text{ yr}^{-1}$  (Haas et al. 2012) (henceforth referred to as HSBL12), producing strong bursts of radiation useful for detecting these events.

The mass function of IMBHs is uncertain but anticipated to be about  $2 \times 10^7$  to  $4 \times 10^8 \text{ Gpc}^{-3}$  (Baumgardt et al. 2004; MacLeod et al. 2016). WDs for their part, represent the final stellar evolution of stars ranging from about 0.07 to 10 solar masses, and are commonly found in spiral galaxies and globular clusters (Reid 2005; Gerssen et al. 2002).

Less common of course are WD-IMBH interactions, but recent estimates place expected disruption rates at  $500 \text{ yr}^{-1} \text{ Gpc}^{-3}$  (Haas et al. 2012).

One especially intriguing aspect of TDEs that concerns this work is the possibility that tidal compression perpendicular to the orbital plane could trigger explosive thermonuclear reactions and create heavy-ion nuclei if the temperature is raised above  $\sim 3 \times 10^8 \text{ K}$  for He burning or  $\sim 3 \times 10^9 \text{ K}$  for C/O (Luminet & Pichon 1989; Rosswog et al. 2009; Haas et al. 2012; Tanikawa et al. 2017; Kawana et al. 2017). This is a likely outcome if the WD is massive enough and tidal compression strong enough. The compression strength in turn is affected by the periastron radius and black hole mass.

If sufficient amounts of radioactive nuclei, e.g.  $^{56}\text{Ni}$ , are synthesized and dispersed along with the unbound debris, their decay (through the  $^{56}\text{Ni} \rightarrow ^{56}\text{Co} \rightarrow ^{56}\text{Fe}$  chain, which releases  $\sim 1 \text{ MeV}$  gamma-rays) supplies nuclear energy to the ejecta, much of which is absorbed and reprocessed as optical/UV photons. The resulting transient emissions might appear similar to Type Ia supernovae with comparable energy release (MacLeod et al. 2016). These optical transients are accompanied by small ejecta mass ( $\lesssim 1M_{\odot}$ ) and fall-back accretion signatures producing flares and jet emissions that emerge at high X-ray and gamma-ray energies, similar to gamma-ray bursts, but softer in spectrum and longer in time. Shcherbakov et al. (2013), for example, suggest that GRB060218 from the *Swift* GRB catalog might be a viable candidate for a TDE involving a WD and a  $10^4 M_{\odot}$  black hole. If confirmed, the appearance of GRB060218 in a dwarf galaxy at a distance of 150 Mpc would indicate IMBHs are more abundant in the local universe than previously thought, by about an order of magnitude.

On the other hand, less massive WDs or weaker tidal interactions may lead to low-luminosity explosions with incomplete radioactive synthesis, or may not explode at all. Incomplete burning can result in relatively large mass fractions of intermediate mass elements (IMEs) such as  $^{40}\text{Ca}$ ,  $^{44}\text{Ti}$ , and  $^{48}\text{Cr}$ . Holcomb et al. (2013) demonstrated how these elements might be a natural outcome from helium detonations in certain conditions typical of WD-IMBH encounters, with calcium production generally increasing with decreasing stellar density. Sell et al. (2015) used these results to propose the possibility that the disruption of a light WD composed mainly of  $^4\text{He}$  can be a progenitor of calcium-rich gap transients. These systems, typically found in the outskirts of known galaxies, exhibit features similar to Type Ia supernovae, but are faint with high velocities and large calcium abundances (Kasliwal et al. 2012). Disruption from some subset of TDEs involving white dwarfs might produce large quantities of IMEs, offering a possible production mechanism for calcium-rich transients.

Observational evidence for the existence of TDE transients (including heavy iron-group elements, IMEs, fall-back accretion flares) remains uncertain, as does the very existence of IMBHs. Identifying distinguishing features of WD tidal events and providing detailed estimates of the properties of these transients might help constrain the highly uncertain nature of the black hole mass function for masses between stellar and supermassive, and place meaningful constraints on the density of IMBHs in the universe.

In this work we consider the disruption and explosion of  $0.2$  and  $0.6 M_{\odot}$  WDs approaching to within a few Schwarzschild radii of  $10^3 - 10^4 M_{\odot}$  non-rotating IMBHs, performing a series of parameter studies in an effort to clarify under what conditions thermonuclear reactions are activated in these near encounter scenarios. Modeling all of the relevant physics in these systems remains a challenging undertaking, requiring substantial computational resources and fidelity modeling of not just hydrodynamics, but also more generally magnetic fields (as recently reported in Guillochon & McCourt 2017), radiation, and nuclear reactions. Near encounters, such as those considered here, additionally require general relativity. We do not consider magnetic fields or radiation in this work. We do however include general relativistic hydrodynamics, a full relativistic treatment of the black hole gravitational field, and a coupled thermonuclear reaction network with self-consistent burn energy feedback. Nearly all numerical work to date associated with TDEs has relied on Newtonian hydrodynamics and gravity (in many cases augmented by central potentials approximating relativistic corrections). Very few incorporate general relativity which is needed to accurately model ultra-close encounters (Laguna et al. 1993; Kobayashi et al. 2004), but none of that body of work includes nuclear reactions. Our goals are to extend previous work (e.g. Rosswog et al. 2009) (henceforth referred to as RRH09) to the general relativistic regime, scope the strength parameter ranges which result in nuclear burning from close encounters, calculate the synthesis of intermediate to heavy mass elements, and explore disruptions of helium-rich WDs to address whether such events are viable candidates for calcium-rich gap transients.

We begin in Section 2 with a brief discussion of our numerical methods, physical models (hydrodynamics, equation of state, nucleosynthesis), and dynamical mesh strategy needed to approach the high spatial resolution required for nucleosynthesis, particularly along the vertical scale height. Initial data for the WD stellar profiles and their locations,

trajectories, and tidal strength parameters for all of the case studies conducted in the course of this work are specified in Section 3. Our results follow in Section 4, and we conclude with a brief summary in Section 5. Unless otherwise noted, standard index notation is used for labeling spacetime coordinates: repeated indices represent summations, raising and lowering of indices is done with the 4-metric tensor, and Latin (Greek) indices run over spatial (4-space) dimensions.

## 2. METHODS

All of the calculations presented in this work use the COSMOS++ computational astrophysics code (Anninos et al. 2005; Fragile et al. 2012, 2014) to solve the equations of general relativistic hydrodynamics with coupled thermonuclear reactions and energy generation. COSMOS++ is a parallel, multi-dimensional, multi-physics, object-oriented radiation-magnetohydrodynamic code, written to support adaptive structured and unstructured meshes, for both Newtonian and general relativistic astrophysical applications. It was originally written for moving and adaptively refined meshes, and has recently been upgraded to accommodate adaptive polynomial order refinement when using high-order discontinuous finite elements (Anninos et al. 2017). For this work we utilize the High Resolution Shock Capturing (HRSC) scheme using finite volume representation with third-order piecewise-parabolic interpolations for the flux reconstructions, and evolved using a third-order, low-storage Euler time-stepping scheme. We use a Kerr-Schild representation for the static (non-rotating) black hole spacetime in Cartesian coordinates.

### 2.1. Relativistic Hydrodynamics

Ignoring radiation, magnetic fields, and viscous contributions, none of which are exercised in this work, the stress energy tensor simplifies to

$$T^{\alpha\beta} = \rho h u^\alpha u^\beta + P g^{\alpha\beta} , \quad (1)$$

where  $\rho$  is the fluid mass density,  $h = 1 + \epsilon/c^2 + P/(\rho c^2)$  is the specific enthalpy,  $c$  is the speed of light,  $u^\alpha = u^0 V^\alpha$  is the contravariant 4-velocity,  $V^\alpha$  is the transport velocity,  $g_{\alpha\beta}$  is the curvature metric, and  $P$  is the fluid pressure providing closure given an appropriate equation of state (see Section 2.2).

The four fluid equations (energy and three components of momentum) are derived from the conservation of stress energy:  $\nabla_\mu T^\mu_\nu = \partial_\mu T^\mu_\nu + \Gamma^\mu_{\alpha\mu} T^\alpha_\nu - \Gamma^\alpha_{\mu\nu} T^\mu_\alpha = S_\nu$ , where  $\Gamma^\alpha_{\mu\nu}$  are the Christoffel symbols and  $S_\nu$  represent arbitrary source terms. In addition to energy and momentum, we also require an equation for the conservation of mass  $\nabla_\mu(\rho u^\mu) = \partial_0(\sqrt{-g}u^0\rho) + \partial_i(\sqrt{-g}u^0\rho V^i) = 0$ .

Expanding out space and time coordinates, the four-divergence ( $\nabla_\mu T^\mu_\nu = S_\nu$ ) of the mixed index stress tensor is written

$$\partial_0(\sqrt{-g}T^0_\nu) + \partial_i(\sqrt{-g}T^i_\nu) = \sqrt{-g}T^\mu_\sigma \Gamma^\sigma_{\mu\nu} + \sqrt{-g}S_\nu . \quad (2)$$

Defining energy and momentum as  $\mathcal{E} = -\sqrt{-g}T^0_0$  and  $\mathcal{S}_j = \sqrt{-g}T^0_j$ , the equations further take on a traditional transport formulation

$$\partial_0\mathcal{E} + \partial_i(-\sqrt{-g}T^i_0) = -\sqrt{-g}T^\mu_\sigma \Gamma^\sigma_{\mu 0} , \quad (3)$$

or

$$\partial_0\mathcal{E} + \partial_i(\mathcal{E}V^i) + \partial_i(\sqrt{-g}PV^i) = -\sqrt{-g}T^\mu_\sigma \Gamma^\sigma_{\mu 0} , \quad (4)$$

for energy, and

$$\partial_0\mathcal{S}_j + \partial_i(\sqrt{-g}T^i_j) = \sqrt{-g}T^\mu_\sigma \Gamma^\sigma_{\mu j} , \quad (5)$$

or

$$\partial_0\mathcal{S}_j + \partial_i(\mathcal{S}_j V^i) + \partial_i(\sqrt{-g}P g^0_j V^i) = \sqrt{-g}T^\mu_\sigma \Gamma^\sigma_{\mu j} . \quad (6)$$

for momentum, and

$$\partial_0\mathcal{D} + \partial_i(\mathcal{D}V^i) = 0 , \quad (7)$$

for mass conservation, where  $\mathcal{D} = \sqrt{-g}u^0\rho = W\rho$  is the boost density.

Mesh motion is implemented by a straight-forward replacement of generic advective terms

$$\partial_0(\sqrt{-g}T^0_\alpha) + \partial_i(\sqrt{-g}T^i_\alpha V^i) \quad (8)$$

with

$$\partial_0(\sqrt{-g}T^0_\alpha) + \partial_i(\sqrt{-g}T^i_\alpha(V^i - V^i_g)) + \sqrt{-g}T^0_\alpha \partial_i V^i_g , \quad (9)$$

where  $V_g^i$  is the grid velocity, and  $T_\alpha^0$  is used here to represent any evolved field, including  $\mathcal{E}$ ,  $\mathcal{S}_j$ , and  $\mathcal{D}$ . The grid velocity can be set arbitrarily by the user, or computed internally by Lagrangian, softened Lagrangian, or potential relaxing algorithms. At the end of each cycle, the zone objects (consisting of node positions, oriented face area vectors, cell volumes, etc.) are physically moved by projecting the zone-centered grid velocity to the nodes and moving them accordingly to the next time cycle, after which all local zone object elements (including the spacetime metric) are updated.

At the beginning of each time cycle a series of coupled nonlinear equations are solved to extract primitive fields (mass density, internal energy, velocity) from evolved conserved fields (boost density, total energy, momentum), after which the equation of state is applied to compute the thermodynamic quantities: pressure, sound speed and temperature. For Newtonian systems this procedure is straightforward, but relativity introduces a nonlinear inter-dependency of primitives so their extraction from conserved fields requires special (Newton-Raphson) iterative treatment. We have implemented several procedures for doing this, solving one, two, or five dimensional inversion schemes for magneto-hydrodynamics, or a nine dimensional fully implicit method (including coupling terms) when radiation fields are present (Fragile et al. 2012, 2014).

## 2.2. Equation of State

We adopt a 2-component equation of state for this work:

$$P = P_{\text{rad}} + P_{\text{gas}} = a_R T^4 / 3 + (\Gamma - 1) Y \rho T, \quad (10)$$

$$(e - e_{\text{cold}}) = e_{\text{rad}} + e_{\text{gas}} = a_R T^4 + Y \rho T, \quad (11)$$

where thermal radiation and ions both contribute to the energy density ( $e \equiv \rho e$ ) and pressure ( $P$ ). The temperature is calculated from the thermal component of the internal energy density, subtracting off the ‘‘cold’’ energy approximated by the initial barotropic equation of state specifying the initial WD data in the absence of shocks:  $e_{\text{cold}} = K \rho^\Gamma / (\Gamma - 1)$ . Additionally,  $Y$  is defined as

$$Y = \frac{k_b}{m_n} \left( \frac{1}{\mu_W} + N_e \right) \frac{1}{\Gamma - 1}, \quad (12)$$

where  $k_b$  is boltzman’s constant,  $m_n$  is the nucleon mass,  $\mu_W = 1 / \sum_i \rho_i / (\rho A_i)$  is the mean molecular weight formed from isotopic densities,  $A_i$  is the atomic weight of isotope  $i$ ,  $N_e$  is the number of electrons per nucleon, and  $\Gamma = 5/3$  is the adiabatic index. The extraction of temperature from equation (11) follows Haas et al. (2012) (see also Lee et al. 2005), but we have generalized (10) to account for radiation pressure. Haas et al. (2012) demonstrated (as we have here) this simplified multi-component treatment capable of reproducing qualitatively similar phase tracks as more complex degenerate equation of state models (RRH09) for the range and scope of stellar and interaction parameters considered in this work. This approximation might adequately capture hydrodynamic behavior, but it is unclear the extent to which it affects calculations of nuclear burn products, which can be highly sensitive to temperature. We anticipate in related future work to implement a more accurate Helmholtz model and assess sensitivities to equation of state choices.

The nonlinear temperature dependence in equation (11) requires Newton inversion each cycle to solve for the temperature given the fluid density and internal energy. Partial ionization is approximated by interpolating the number of electrons per nucleon  $N_e$  in equation (12), between zero (no ionization) and 1/2 (full ionization), over the range of temperatures  $T = 5 \times 10^5$  to  $T = 5 \times 10^6$  K. The mean molecular weight  $\mu_W$  is updated each cycle from the isotopic fractions produced after solving the nuclear reaction network discussed in the following section.

## 2.3. Nuclear Network

COSMOS++ supports a number of nuclear reaction networks, including the 7- and 19-isotope  $\alpha$ -chain and heavy-ion reaction models developed by Weaver et al. (1978), Timmes (1999) and Timmes et al. (2000). There is of course a trade-off between speed versus accuracy as measured by nuclear energy production when choosing between these two networks. Timmes et al. (2000) report 30-40% differences in energy production rates from the two models across different stellar environments and burn stages. We find the more accurate 19-isotope model imposes a tolerable increase in computing time, so we adopt that network for this work. The 19-isotope network solves heavy-ion reactions using a standard  $\alpha$ -chain composed of 13 nuclei ( $^4\text{He}$ ,  $^{12}\text{C}$ ,  $^{16}\text{O}$ ,  $^{20}\text{Ne}$ ,  $^{24}\text{Mg}$ ,  $^{28}\text{Si}$ ,  $^{32}\text{S}$ ,  $^{36}\text{Ar}$ ,  $^{40}\text{Ca}$ ,  $^{44}\text{Ti}$ ,  $^{48}\text{Cr}$ ,  $^{52}\text{Fe}$ , and  $^{56}\text{Ni}$ ), plus additional isotopes ( $^1\text{H}$ ,  $^3\text{He}$ ,  $^{14}\text{N}$ ,  $^{54}\text{Fe}$ ) to accommodate some types of hydrogen burning as well as photo-disintegration neutrons and protons.

To account for the advection of reactant species, the hydrodynamic equations described in Section 2.1 are supplemented with an additional set of mass continuity equations, one for each isotope  $j$  in the network, resulting in the following 19 partial differential equations that need to be solved each advance cycle:

$$\partial_0(W\rho_j) + \partial_i(W\rho_j V^i) = \sum_{k,l,m} \rho_m \rho_l R_{lk}(m) - \rho_j \rho_k R_{kl}(j) . \quad (13)$$

Equation (13) is written in simplified form explicitly for, but not limited to, binary reactions, where  $R_{lk}(m)$  represents creation rates contributed by species  $m$ , and  $R_{kl}(j)$  are the corresponding destruction rates for species  $j$ . These rate coefficients are highly nonlinear in temperature and span many orders of magnitude. As a result, the differential equations for the reaction network (the ODEs consisting of the right-hand-side of equation (13) after operator splitting off advection) are stiff and must be solved with implicit or semi-implicit integration methods. We have implemented a number of solvers and evaluated their performance in some of our tidal event calculations, including 4th, 5th and 8th order explicit and semi-implicit adaptive timestep Runge-Kutta schemes, the variable order Bader-Deufelhard method, and a 5th order fully implicit method. The fully implicit solver proved faster and more robust for this class of problems, completing the 3D calculations faster (by a factor of several) and with fewer (by a factor of three) first-attempt network convergence failures than its closest competitor (Bader-Deufelhard).

Network failures occur when the solver does not converge to a user-specified fractional tolerance for each species abundance, which we set to  $10^{-6}$ . When the solver fails to meet this tolerance over a full hydrodynamic cycle, that particular zone is flagged and switched over to a sub-cycling method where the time step is systematically reduced until the solver converges. The equation of state is re-calculated consistently at each sub-cycle as is the internal energy production, properly updating the temperature and reaction rates before each new sub-cycled reaction solve. The local minimum time step needed for proper convergence is recorded and used to set the global timestep for the next hydrodynamic cycle. The global time step is also constrained to limit relative energy production to 25% fractional change. These highly restrictive conditions are necessary for achieving stable and accurate solutions since nuclear reaction time steps can easily become much smaller than hydrodynamic time scales.

The specific energy released by nuclear reactions is calculated from

$$\delta\epsilon_{\text{nuc}} = N_A \sum_j B_j \delta Y_j , \quad (14)$$

where  $N_A$  is Avogadro's number,  $B_j$  is the binding energy, and  $Y_j$  is the dimensionless molar abundance of isotope  $j$ . It is defined in terms of the mass fractions  $X_j = \rho_j/\rho$ , atomic weights  $A_j$  (proton + neutrons), total mass density  $\rho$ , and number densities  $n_j$  as  $Y_j = X_j/A_j = \rho_j/(\rho A_j) = n_j/(\rho N_A)$ . The corresponding internal energy change (accumulated over all subcycled intervals)  $\delta e = \rho \delta\epsilon_{\text{nuc}}$  is then used to update the relativistic momentum and total energy fields, after also updating the pressure change  $\delta P$  from the equation of state

$$\mathcal{E}^{n+1} = \mathcal{E}^n - ((\delta e + \delta P)Wu_0 + \sqrt{-g} \delta P) , \quad (15)$$

$$\mathcal{S}_j^{n+1} = \mathcal{S}_j^n + (\delta e + \delta P)Wu_j . \quad (16)$$

In this formulation, we have assumed the WD material is sufficiently optically thick (to photons and neutrons), that released energy can not be radiated away and is instead absorbed instantaneously in cells where it has been emitted.

Performance of the reaction solver and nuclear energy production model have been validated against the entire suite of problems and code tests proposed by Timmes et al. (2000), in addition to adiabatically coupled nuclear flows (e.g., standard Big Bang nucleosynthesis). The hydrodynamic coupling and subcycling procedure are identical to the methods we had previously developed and vetted for chemical reactive networks with radiative cooling, and have subjected them to numerous tests, including self-similar reactive flows, molecular species formation in cosmological shocks, and hydrodynamic shock masking. We have here only substituted nuclear rates for chemical.

#### 2.4. Mesh Kinetics

All simulations use a 3D Cartesian grid centered on the WD, covering a spatial domain of  $2R_{\text{WD}}$  along the  $z$ -axis and  $4R_{\text{WD}}$  in the  $x - y$  orbital plane, where  $R_{\text{WD}}$  is the radius of the white dwarf. For most of our calculations, the domain is resolved with three hierarchical grid layers with  $96^3$  cells on the base level and two additional refinement levels (each level doubling the resolution) for an effective  $384^3$  resolution covering the star. For a WD with radius  $10^9$



cm, this results in an initial uniform cell resolution  $(\Delta x, \Delta y, \Delta z)$  of  $\sim (2.1, 2.1, 1.1) \times 10^7$  cm or in terms of scaled dimensions  $\sim (R_{S,3}/15, R_{S,3}/15, R_{S,3}/30)$ , where  $R_{S,3}$  is the Schwarzschild radius for a  $10^3 M_\odot$  black hole. Adaptive mesh refinement (AMR) is used throughout the calculations, refining and de-refining every five hydrodynamic cycles. AMR is triggered by the local mass density, refining where the density exceeds  $\rho_{\max}/20$ , de-refining where the density drops below  $\rho_{\max}/200$ , where  $\rho_{\max}$  is the initial maximum cell density across the grid.

Since the TD events considered here have much in common with our earlier work on the disruption of the G2 cloud orbiting our galactic center (Anninos et al. 2012), we adopt a similar approach for implementing a grid velocity to track the trajectory of the WD. Grid velocity is used to move the base grid at the mean (density weighted) Lagrangian velocity of the star, following its orbital motion in the  $x - y$  orbital plane while keeping the star centered on the grid. Adaptive mesh refinement is performed on the moving base mesh. The combination of grid velocity and AMR together allows us to use fewer refinement levels to achieve high resolution across the stars throughout their evolution. By comparison, HSBL12 built 8 levels of refinement to achieve comparable resolution. We note however that we additionally improve on the vertical scale height resolution as described next.

Because the WD is compressed along the  $z$ -axis, perpendicular to the orbital plane, mesh motion along that direction requires special treatment. Tanikawa et al. (2017) argued the importance of capturing shocks within the scale height of the WD to resolve nuclear explosions. Estimating the scale height  $z_{\min}$  of the WD in the  $z$ -direction as  $z_{\min}/R_{\text{WD}} \sim \beta^{-2/(\Gamma-1)}$  at periapsis, where  $\beta$  is the tidal strength parameter defined in the next section (Luminet & Carter 1986; Brassart & Luminet 2008; Tanikawa et al. 2017), we anticipate a WD with an initial radius of  $10^9$  cm will require a cell resolution of about  $10^6$  cm in a tidal field with  $\beta = 10$ . We therefore augment the orbital mesh velocity by introducing a converging component toward the  $z = 0$  plane with magnitude

$$|V_g^z(t)| = \zeta_2 |V_L^z(t)| \left| \frac{z(t)}{L_z(t)} \right|^{\zeta_N}, \quad (17)$$

where  $z(t)$  is the time-dependent coordinate,  $L_z(t)$  is the changing vertical length of the grid along the positive  $z$ -axis (distance from the orbital plane to the outer boundary),  $\zeta_2 \geq 0$  is a constant multiplier, and  $|V_L^z(t)|$  is the average magnitude of the downward-directed  $z$ -component of the star's internal Lagrangian velocity. The factor  $|z(t)/L_z(t)|^{\zeta_N}$  smoothly scales back the vertical grid motion to zero at the midplane, preventing mesh singularities from forming. Large values of the exponent  $\zeta_N > 1$  tend to collapse the outer grid edges faster than the midplane cells. Fractional values  $0 < \zeta_N < 1$  tend to collapse the midplane zones at a faster rate. We choose  $\zeta_N = 0.85$  as a reasonable compromise. The multiplier  $\zeta_2$  is initially set to 5 but deactivated (reset to zero) when the vertical scale height resolution improves ten-fold to  $\sim 10^6$  cm or equivalently  $R_{S,3}/300$ . This prescription allows the innermost and outermost cells to move inward towards the orbital plane at different velocities, collapsing the inner zones by a factor of ten, while cutting the distance to the outer  $z$ -boundary planes by about two-thirds, depending on specific case parameters.

When the WD passes periapsis, grid motion in the  $x - y$  plane is modified to keep both the star and black hole on the grid for the remaining evolution to capture flow circulation. This is accomplished by continuing to track the orbital velocity of the star, while also allowing the grid to stretch according to

$$V_g^x = \min(0, v_L^x(t)) \frac{x_{\max}(t) - x(t)}{x_{\max}(t) - x_{\min}(t)} \quad (18)$$

$$V_g^y = \min(0, v_L^y(t)) \frac{y_{\max}(t) - y(t)}{y_{\max}(t) - y_{\min}(t)}, \quad (19)$$

where  $x_{\max/\min}(t)$  and  $y_{\max/\min}(t)$  are the evolving maximum/minimum  $x$  and  $y$  grid positions. This choice of grid velocity holds the upper right edge of the grid fixed to retain the black hole on the grid, while allowing the lower left edge to stretch with the tidal debris and approximately track the stellar centroid as it flows past and around the black hole.

The boundary conditions on the outer edges of the grid are set to outflow conditions. All ghost zone quantities are equated to the values of their adjacent internal-zone neighbors, except the velocity component normal to the boundary is set to zero if it points onto the grid. Note, this does not necessarily prevent material from coming onto the grid as the parabolic reconstruction of the fluxes may still produce negative or positive values.

### 3. INITIAL DATA

There are a few important physical quantities that characterize WD-IMBH systems. First the radius of a non-rotating Schwarzschild black hole,  $R_S = 2GM_{\text{BH}}/c^2 \approx 3 \times 10^8 (M_{\text{BH}}/10^3 M_\odot)$  cm, where  $M_{\text{BH}}$  is the black hole mass. Second, the tidal radius  $R_T$  at which the tidal force exceeds self-gravity

$$R_T \approx 1.2 \times 10^{10} \left( \frac{R_{\text{WD}}}{10^9 \text{cm}} \right) \left( \frac{M_{\text{BH}}}{10^3 M_\odot} \right)^{1/3} \left( \frac{M_{\text{WD}}}{0.6 M_\odot} \right)^{-1/3} \text{ cm} , \quad (20)$$

where  $R_{\text{WD}}$  is the WD radius, and  $M_{\text{WD}}$  is the WD mass. From these two quantities, together with the periapsis radius  $R_P$ , one can define several dimensionless parameters representing the strength of the tidal encounter  $\beta = R_T/R_P$ , the condition under which the WD will be swallowed by the black hole without leaving unbound traces  $\beta_S = R_T/R_S$ , and the condition under which the BH will swallow a part of the WD in the first passage (the so-called ‘‘WD swallowing the BH limit’’)  $\beta_{\text{WD}} = R_T/R_{\text{WD}}$ . Expressions for the latter two quantities take the following approximate form:

$$\beta_S \approx 40 \left( \frac{R_{\text{WD}}}{10^9 \text{cm}} \right) \left( \frac{M_{\text{BH}}}{10^3 M_\odot} \right)^{-2/3} \left( \frac{M_{\text{WD}}}{0.6 M_\odot} \right)^{-1/3} , \quad (21)$$

$$\beta_{\text{WD}} \approx 12 \left( \frac{M_{\text{BH}}}{10^3 M_\odot} \right)^{1/3} \left( \frac{M_{\text{WD}}}{0.6 M_\odot} \right)^{-1/3} . \quad (22)$$

A WD is tidally disrupted if  $\beta \geq 1$ , is not swallowed entirely by the BH if  $\beta \leq \beta_S$ , and avoids swallowing the BH (or equivalently avoiding the BH swallowing part of the WD at first passage) if  $\beta \leq \beta_{\text{WD}}$ . Additionally, one can easily derive an expression for the maximum BH mass  $M_{\text{BH,max}}$  above which tidal disruption is ineffective by setting  $\beta_S = 1$  and solving for  $M_{\text{BH}}$

$$M_{\text{BH,max}} = 2.5 \times 10^5 \left( \frac{R_{\text{WD}}}{10^9 \text{cm}} \right)^{3/2} \left( \frac{M_{\text{WD}}}{0.6 M_\odot} \right)^{-1/2} M_\odot . \quad (23)$$

Equation (23) clearly shows that supermassive BHs (masses greater than  $\sim 10^5 M_\odot$ ) are not good tidal encounter candidates for white dwarfs.

Initial data for the stars are derived by solving the relativistic Tolmon-Oppenheimer-Volkof (TOV) equations with polytropic constant  $K = P\rho^{\Gamma-1} = 4.45 \times 10^{-9} (\text{g/cm}^3)^{(1-\Gamma)}$  with  $\Gamma = 5/3$ . These solutions produce  $0.6(0.2)M_\odot$  WDs with radii  $1.3(1.8) \times 10^9$  cm, central densities  $7.2 \times 10^5 (1.1 \times 10^5)$  g cm $^{-3}$ , central pressures  $2.3 \times 10^{22} (1.0 \times 10^{21})$  erg cm $^{-3}$ , and total internal energies  $3.1 \times 10^{49} (3.4 \times 10^{48})$  erg. We have also computed  $0.2$  and  $0.6 M_\odot$  WD solutions using the MESA stellar evolution code (Paxton et al. 2011) to derive initial isotopics providing more realistic distributions than the uniform and single (or dual) species assumptions often invoked in the literature. For the  $0.2 M_\odot$  case, a uniform distribution composed mostly of  $^4\text{He}$  across the entire radius of the WD is actually a fair approximation; MESA predicts a 99% mass fraction of helium, with trace amounts of hydrogen, carbon, nitrogen, oxygen, neon, and magnesium. The  $0.6 M_\odot$  WD however exhibits a more complex substructure characterized by four distinct layers as shown in Figure 1. The inner half of the WD is roughly a homogeneous mixture of  $1/3$   $^{12}\text{C}$  and  $2/3$   $^{16}\text{O}$  (with trace amounts of heavier nuclei), surrounded by carbon-rich, helium-rich, and hydrogen-rich layers, ordered from the inner core to the outer surface.

A few considerations define our choice for the background gas. First, we assume the background gas is composed of hydrogen and helium in primordial abundance. Second, we require the mass density be small and not contribute significantly to the mass accretion rates, but not too low that the resulting sound speed dominates the compute cycle. We choose  $\rho_{\text{gas}} = 10^{-7} \rho_c$  as a reasonable compromise, where  $\rho_c$  is the initial central density in the WD. Third, we require the pressure in the background gas does not produce strong thermodynamic response from the WD prior to disruption. Large pressure gradients across the stellar surface can produce bow shocks around the leading surface of the star as it moves through the BH environment. Additionally, high background pressures increase the sound speed and slow the compute cycle. We set the background pressure to the star surface pressure defined at  $5 \times 10^{-4}$  of the peak central density. At these background temperatures and densities, the WD response is dominated by tidal interactions, not pressure or inertial forces at the surface, even though both the WD and mesh move supersonically through the background.

All calculations begin with the WD positioned in the  $x-y$  orbital plane on parabolic trajectories defined by periapsis radius  $R_P$  and initial time specified in terms of the characteristic orbital time  $\tau_{\text{orb}} = 2\pi R_P \sqrt{R_P/GM_{\text{BH}}}$  from periapsis

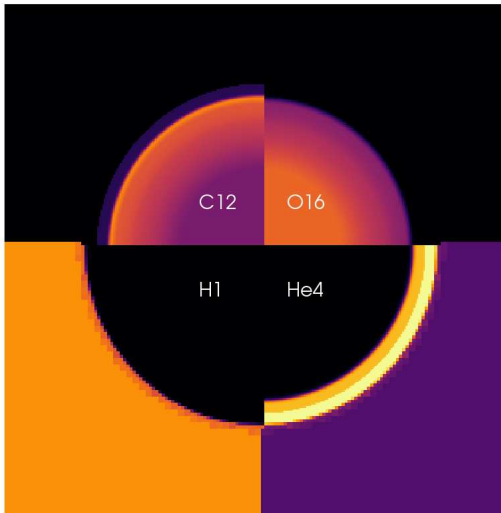


**Figure 1.** Initial mass fractions of the four dominant isotopes in the interior of the  $0.6M_{\odot}$  WD. The four isotopes are layered roughly into four distinct regions: an oxygen-rich center that transitions to a carbon-rich middle layer, then respectively to thinner helium and hydrogen outer layers. The background environment is hydrogen/helium gas in primordial abundance. Color maps are all normalized to the same linear scale from zero (black) to one (yellow).

at  $t = 0$ . Since all simulations start before periastris passage, the initial  $t$  is negative. Flexibility in the choice of initial times is used to position stars that are on different trajectories to comparably scaled distances from the black hole, approximately one tidal radius so we can reasonably neglect self-gravity of the WD. Due to the computationally demanding nature of the calculations (particularly when nuclear reactions are strongly activated, which can easily increase cycle times by factors of a few), all runs are terminated one to two seconds after the WD passage through periastris, after nucleosynthesis completes at energy production levels of  $\delta e_{\text{nuc}}/(e \delta t) < 0.01$ , but before circularization fully develops.

Although self-gravity is neglected in many of our calculations, we have run several models with a Cowling approximation to self-gravity, adding the TOV calculated potential as a perturbative correction to the black hole spacetime metric, centered on the evolving WD centroid. We find our results are relatively insensitive to this treatment, which is not surprising considering the contribution to the local gravitational potential is more than an order of magnitude smaller than the central potential contribution from the black hole at distances within where the stars are initialized. In addition, the expansion time scale (when self-gravity is neglected) as estimated by the ratio of the star’s diameter to the maximum sound speed is also nearly an order of magnitude greater than the time interval to travel from unit tidal radius to where tidal forces are clearly dominant. These conclusions are born out in the numerical calculations. With the neglect of self-gravity we find stars expand not more than 10% from their initial radius. The impact on our final results are equivalently small: Total nuclear energy production and iron-group abundances differ only by 10% with and without self-gravity. Similar behavior is observed when we neglect self-gravity and instead place the stars at half the tidal radius, in which case there is no opportunity for the stars to expand before they are immediately disrupted by the BH.

We have additionally placed stars at twice and three times the temporal tidal distance from the BH to quantify the impact that early (pre-tidal phase) distortions might have on nucleosynthesis. Here our findings are less conclusive. The Cowling approximate potential is unable to maintain precise enough equilibrium through that long a trajectory. The star radius measured along the vertical direction expands by a considerable amount, more than 20%, before compression from the black hole begins to dominate. We thus have two competing forces outside the tidal radius



**Table 1.** Run Parameters

Run	$M_{\text{BH}}$ ( $M_{\odot}$ )	$M_{\text{WD}}$ ( $M_{\odot}$ )	$R_{\text{P}}$ ( $R_{\text{S}}$ )	$R_{\text{WD}}$ ( $R_{\text{S}}$ )	$R_0$ ( $R_{\text{S}}$ [ $R_{\text{T}}$ ])	$\beta$
B3M2R28	$10^3$	0.2	28	6.1	98 [0.99]	3.5
B3M2R24	$10^3$	0.2	24	6.1	98 [0.99]	4.1
B3M2R22	$10^3$	0.2	22	6.1	98 [1.03]	4.3
B3M2R20	$10^3$	0.2	20	6.1	104 [1.04]	5.0
B3M2R09	$10^3$	0.2	9	6.1	97 [0.97]	11
B3M2R06	$10^3$	0.2	6	6.1	93 [0.93]	17
B3M6R20	$10^3$	0.6	20	4.4	53 [1.00]	2.6
B3M6R12	$10^3$	0.6	12	4.4	49 [1.10]	4.5
B3M6R09	$10^3$	0.6	8	4.4	59 [1.10]	5.9
B3M6R06	$10^3$	0.6	6	4.4	57 [1.06]	8.9
B4M2R06	$10^4$	0.2	6	0.61	21 [1.02]	3.4
B4M2R04	$10^4$	0.2	4	0.61	19 [0.90]	5.4
B3M6R20-L2	$10^3$	0.6	20	4.4	53 [1.00]	2.6
B3M6R20-L1	$10^3$	0.6	20	4.4	53 [1.00]	2.6
B3M6R12-L2	$10^3$	0.6	12	4.4	49 [1.10]	4.5
B3M6R12-L1	$10^3$	0.6	12	4.4	49 [1.10]	4.5
B3M6R06-L2	$10^3$	0.6	6	4.4	57 [1.06]	8.9
B3M6R06-L1	$10^3$	0.6	6	4.4	57 [1.06]	8.9

conspiring to distort the stars: One physical due to the black hole, one artificial due to the neglect of (or inadequate) self-gravity. Both act to decrease the efficiency of nuclear activity. We get a sense of the proportion of these two effects by estimating the time scale for each. Comparing the expansion time  $T_{\text{exp}} \sim 2R_{\text{WD}}/c_s$  (where  $c_s$  is the peak or central sound speed inside the WD) against the tidal disruption time  $T_{\text{tde}} \sim \sqrt{R_0^3/GM_{\text{BH}}}$ , we find they are roughly equal at distances between one to two tidal radii. Hence attributing the differences we observe in nuclear activity (both energy and iron-group production) equally to tidal disruption and thermal expansion, we estimate that the neglect of early-time distortion affects our results by about 25%, significantly more than the neglect of self-gravity inside the tidal radius. We are thus effectively under-predicting nuclear activity 10% by neglecting self-gravity inside the tidal radius, but also over-predicting activity 25% by neglecting tidal effects outside the tidal radius. Collectively these two competing effects contribute to an uncertainty of 15% in our nuclear diagnostics, not entirely negligible but still nonetheless smaller than the sensitivity we observe with spatial resolution.

Table 1 and Figure 2 summarize the models we consider in this report, exploring three main parameters: black hole mass  $M_{\text{BH}}$ , white dwarf mass  $M_{\text{WD}}$ , and relativistic domain quantified by the periastron radius  $R_{\text{P}}$ . Each of these parameters are conveniently encapsulated in the run labels. For example run B3M2R28 signifies a black hole mass of  $10^3 M_{\odot}$  (B3), a WD mass of  $0.2 M_{\odot}$  (M2), and perihelion radius of  $28 R_{\text{S}}$  (R28). Also displayed in the table are the radius of the white dwarf  $R_{\text{WD}}$ , initial distance  $R_0$  from the black hole in units of the Schwarzschild and tidal radii, and tidal strength  $\beta$ . As mentioned earlier, most of our calculations are performed on a 3-level hierarchical grid with a  $96^3$  base mesh and two additional layers of refinement, but we have also run some calculations at lower resolution (labeled -L2 and -L1 in the table for 2-level and 1-level grids respectively) to assess convergence. The tidal strength parameter  $\beta$  is a derived quantity whose range is restricted by the combination of black hole mass and  $R_{\text{P}}$ . The choice  $10^{3-4} M_{\odot}$  for the black hole mass accommodates a broad range of  $\beta$  as  $R_{\text{P}}$  approaches the Schwarzschild radius. We do not consider lower mass black holes because we want to avoid the  $\beta_{\text{WD}}$  limit where the WD swallows the black hole in near encounters (essentially keeping  $R_{\text{WD}} < R_{\text{P}}$  when  $R_{\text{P}} \sim R_{\text{S}}$ ). Higher mass black holes approach the  $\beta_{\text{S}}$  limit, which results in weaker tidal interactions generally incapable of triggering nucleosynthesis.

#### 4. RESULTS

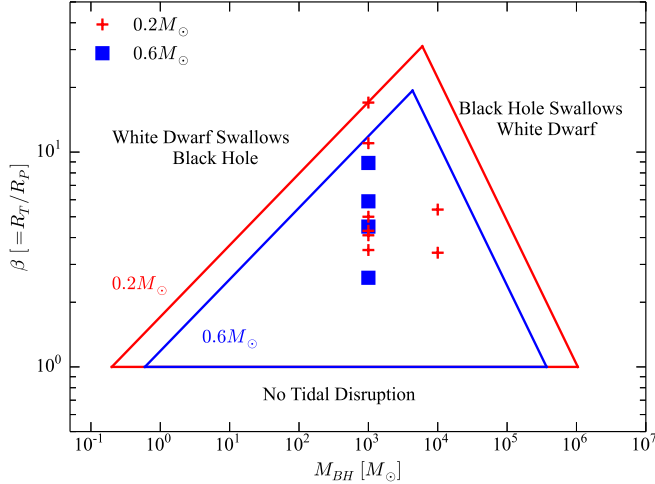


**Figure 2.** Parameter space associated with tidal disruption of 0.2 (red) and  $0.6M_\odot$  (blue) white dwarfs. Symbols indicate parameter combinations considered in this paper.

#### 4.1. Hydrodynamics

Several deformation modes are active during typical disruption encounters. In the  $x$ - $y$  orbital plane of the binary system, the star will experience tidal stretching along the direction connecting the black hole to the WD, and tidal compression perpendicular to this direction. The star will also undergo tidal compression in the direction perpendicular to the orbital plane. Compression perpendicular to the orbital plane is significantly greater than that in the orbital plane, and is the primary mechanism that could, in principle, ignite nuclear reactions in the WD. These deformation modes are demonstrated in Figures 3 and 4, which image the logarithm of mass density and temperature in the  $x$ - $y$  (orbital) and  $y$ - $z$  planes for run B3M2R06. Stretching and compression in the orbital plane are both evident in the series of images in Figure 3, conspiring to simultaneously thin and elongate the WD in orthogonal directions whose orientations change as the WD approaches the BH. Compression acting perpendicular to the orbital plane is on display in Figure 4, where the WD collapses to a fraction of its original size. Both figures demonstrate the effectiveness of the mesh velocity prescription described in Section 2.4 to track the orbital trajectory and at the same time collapse the grid in response to tidal compression along the vertical direction. Figures 3 and 4 are representative of all encounter scenarios we have studied in that nuclear burning is not triggered and thus has little effect on stellar disruption until the approach and passage of periastris. Ignition is triggered mainly along the dense filamentary-like nozzle structure that forms where the stellar material is pinched to maximal compression as it passes periastris, and is clearly evident in the third panels of Figure 3 projecting radially outward from the black hole. Apart from the creation of burn products, the important hydrodynamical effect of nuclear ignition is the deposition of released energy which contributes to the overall disruption of the WD.

We attribute the small scale structures present in the third panel of Figure 3 to transitory hydrodynamic instabilities. Material compressing onto the orbital plane before reaching the nozzle is stable, but as Figure 11 shows, this material bounces after passing through the nozzle and accelerates outward from the orbital plane, reversing the direction of its vertical velocity and reshocking as it hits infalling material. In addition, the infalling material is not perfectly aligned with the dense thin shell of material forming along the nozzle, which creates tangentially aligned streamlines within the dense layer that can potentially induce perturbations (though we cannot conclusively say this actually happens due to the lack of sufficient orbital plane resolution). In all, this creates an interpenetrating, multi-shock morphology inside the disrupted star that gives rise to interspersed Rayleigh-Taylor unstable regions and strong shear flows that also trigger Kelvin-Helmholtz instabilities. The result is a complex flow pattern downstream of the nozzle characterized by debris separation into filamentary structures. We have verified these features are robust (present) regardless of numerical treatments, including activation of AMR, mesh motion, thermonuclear reactions, or equation of state (they are present even with a simple ideal gas law with no ionization temperature thresholds). These features, however, are strongly sensitive to grid resolution and are less pronounced when the central plane is inadequately resolved. In fact when we increase resolution, the structures become more coherent, numerous, smaller in scale, and we expect this

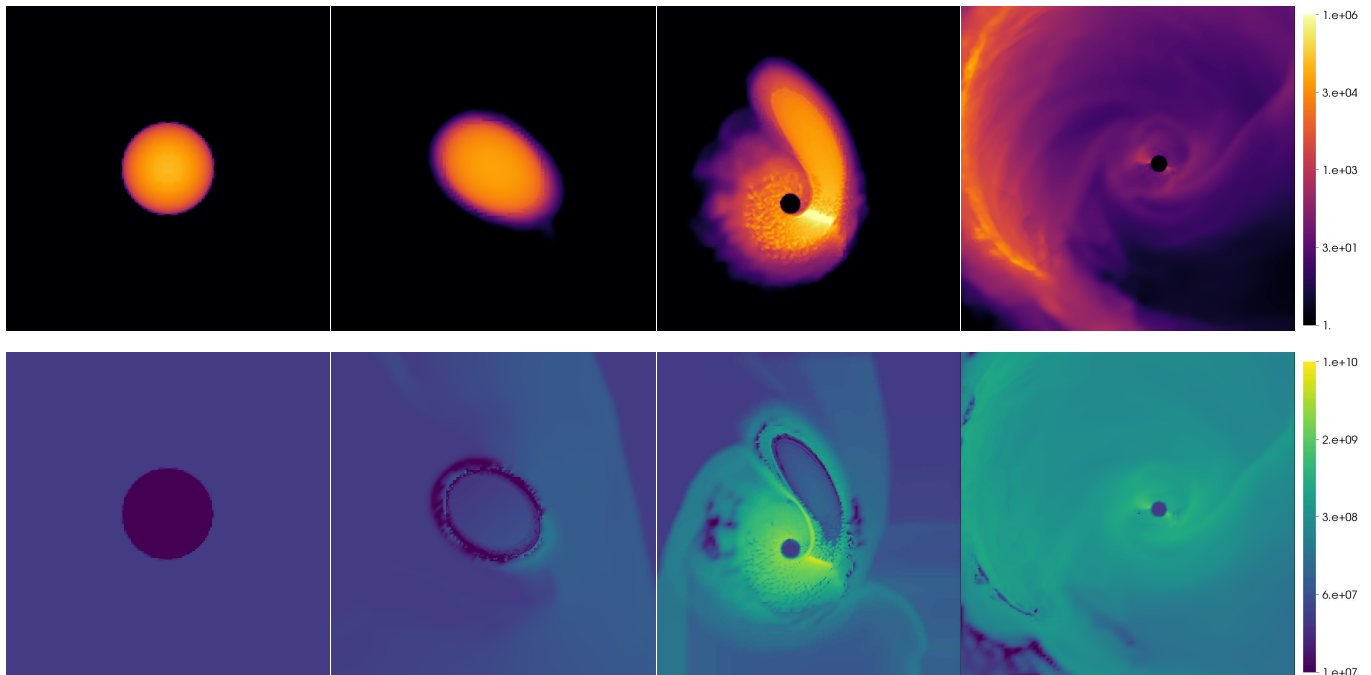


**Figure 3.** Logarithm of the mass density (in  $\text{g cm}^{-3}$ , top) and temperature (in K, bottom) from the B3M2R06 run plotted in the orbital  $x$ - $y$  plane at  $t = -6.4, -2.0, 0.0,$  and  $2.0$  s. The entire cross section of the grid is shown in each frame, but its linear scale changes.

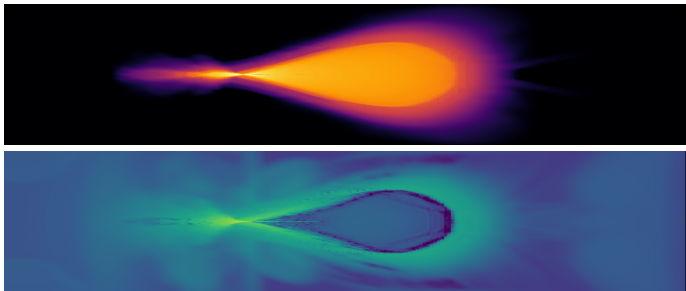


**Figure 4.** Logarithm of the mass density (in  $\text{g cm}^{-3}$ , top) and temperature (in K, bottom) from the B3M2R06 run plotted in the  $y$ - $z$  plane near periaapsis at  $t = 0.0$  s. The entire cross section of the grid is shown in each frame, nicely illustrating the star and grid compression in the  $z$ -direction. The color scale is the same as in Fig. 3.

trend to continue at resolutions beyond our current limits. Upon close inspection these features are evident also in the work of other authors (see for example Kawana et al. (2017)), but they are more pronounced in our calculations due to increased spatial resolution and perhaps our use of less dissipative, high order shock capturing numerical methods. Although we can say with some degree of confidence these structures are to be expected, clearly more careful and much higher resolution studies will be needed to better understand their cause and effects.

In general, and as expected, we find more massive WDs compress to greater densities and temperatures, as do WDs on trajectories approaching closer to the black hole. The density-temperature phase tracks calculated for the densest 10% of stellar material and plotted in Figure 5 demonstrate this for a few cases involving encounters with a  $10^3 M_\odot$  black hole. Notice the positive correlation of increasing compression and heating with decreasing perihelion radius. Also shown in this figure is the curve separating dynamical and helium burn reaction timescales. If the dynamical time scale  $\tau_D = 1/\sqrt{G\bar{\rho}_{\text{WD}}}$  is shorter than the helium combustion timescale  $\tau_B \approx 9 \times 10^{-4} (T_9)^3 (\rho_6)^{-2} \exp[4.4/(T_9)]$  s (Khokhlov & Ergma 1986), where  $\bar{\rho}_{\text{WD}}$  is the mean WD density,  $T_9 = T/10^9$  K, and  $\rho_6 = \rho/10^6$   $\text{g cm}^{-3}$ , the star can expand rapidly enough to quench burning by cooling the WD interior and reducing its density. Most of the cases we have studied track into the fast combustion timescale regime, achieving density compression ratios of more than an order of magnitude and temperatures exceeding those needed to burn carbon-oxygen chains. The maximum densities

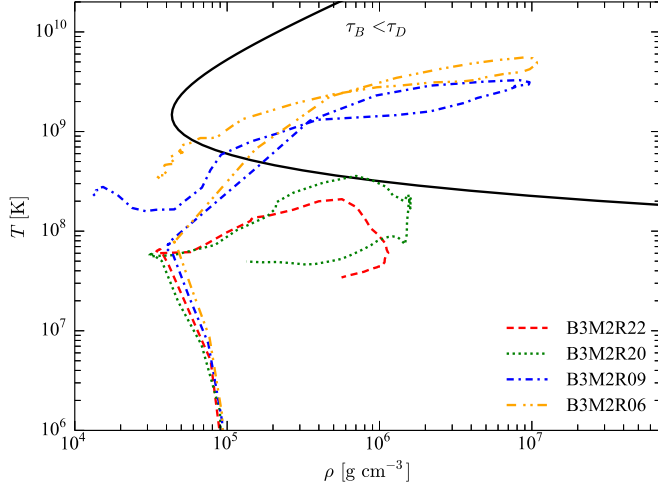


**Figure 5.** Density-temperature tracks for  $0.2M_{\odot}$  WD encounters with a  $10^3M_{\odot}$  black hole. The data represent density-weighted averages from the densest 10% of stellar matter. The solid black curve is where helium combustion and dynamical reaction time scales equate. Regions above this curve burn at rates faster than hydrodynamical cooling effects can suppress nuclear burn.

**Table 2.** Result Summary

Run	$\rho_{\max}$ ( $\text{g cm}^{-3}$ )	$T_{\max}$ (K)	$\epsilon_{\text{nuc}}$ (erg)	$M_{\text{Fe,max}}$ ( $M_{\odot}$ )	$M_{\text{Ca,max}}$ ( $M_{\odot}$ )
B3M2R28	$4.5 \times 10^5$	$1.4 \times 10^8$	$1.3 \times 10^{47}$	$< 10^{-15}$	$< 10^{-15}$
B3M2R24	$9.1 \times 10^5$	$1.4 \times 10^8$	$5.6 \times 10^{47}$	$< 10^{-15}$	$1 \times 10^{-14}$
B3M2R22	$1.2 \times 10^6$	$2.1 \times 10^8$	$1.6 \times 10^{48}$	$< 10^{-15}$	$9 \times 10^{-11}$
B3M2R20	$1.7 \times 10^6$	$3.7 \times 10^8$	$2.9 \times 10^{49}$	0.0034	0.0034
B3M2R09	$1.1 \times 10^7$	$3.4 \times 10^9$	$3.1 \times 10^{50}$	0.0891	0.0065
B3M2R06	$1.2 \times 10^7$	$5.8 \times 10^9$	$2.8 \times 10^{50}$	0.0798	0.0030
B3M6R20	$2.0 \times 10^6$	$5.2 \times 10^8$	$1.4 \times 10^{49}$	0.0001	0.0002
B3M6R12	$9.5 \times 10^6$	$1.1 \times 10^9$	$1.6 \times 10^{50}$	0.0008	0.0045
B3M6R09	$3.0 \times 10^7$	$4.1 \times 10^9$	$7.6 \times 10^{50}$	0.2646	0.0154
B3M6R06	$7.2 \times 10^7$	$9.0 \times 10^9$	$8.7 \times 10^{50}$	0.3690	0.0094
B4M2R06	$3.2 \times 10^5$	$2.7 \times 10^8$	$7.1 \times 10^{48}$	$< 10^{-15}$	$5 \times 10^{-12}$
B4M2R04	$6.0 \times 10^5$	$1.1 \times 10^9$	$1.1 \times 10^{50}$	0.0017	0.0306
B3M6R20-L2	$1.9 \times 10^6$	$4.7 \times 10^8$	$1.2 \times 10^{49}$	$2 \times 10^{-15}$	$8 \times 10^{-11}$
B3M6R20-L1	$1.6 \times 10^6$	$3.9 \times 10^8$	$7.8 \times 10^{48}$	$2 \times 10^{-15}$	$1 \times 10^{-12}$
B3M6R12-L2	$8.2 \times 10^6$	$1.7 \times 10^9$	$1.7 \times 10^{50}$	0.0016	0.0048
B3M6R12-L1	$6.0 \times 10^6$	$1.7 \times 10^9$	$1.6 \times 10^{50}$	0.0006	0.0018
B3M6R06-L2	$4.0 \times 10^7$	$7.9 \times 10^9$	$7.8 \times 10^{50}$	0.3548	0.0128
B3M6R06-L1	$1.8 \times 10^7$	$6.5 \times 10^9$	$7.1 \times 10^{50}$	0.3171	0.0170

and (separately) temperatures observed in our parameter studies are summarized in Table 2. The resolution case studies of B3M6R20, R12, and R06 collectively suggest that the peak densities and temperatures are converged to about 20%. This might be adequate if the only consideration was hydrodynamic behavior or global nuclear energy production (see section 4.2). However, nuclear reaction rates are highly sensitive to temperature and we find somewhat greater uncertainty in the isotopic distributions as discussed in more detail below.

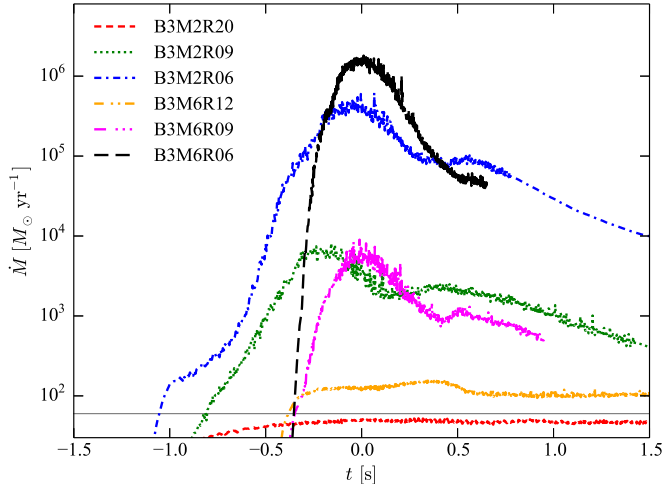


**Figure 6.** Mass accretion rates for 0.2 and 0.6  $M_{\odot}$  WD encounters with a  $10^3 M_{\odot}$ . All profiles exhibit similar distinct features: an early large amplitude burst centered at periapsis ( $t \sim 0$  s), followed by a quasi-static phase characterized by a much shallower temporal decay. The horizontal gray line near the bottom of the plot estimates the background mass accretion rate.

Mass accretion rates are plotted as a function of time in Figure 6 for a sample of cases. There are two distinct signature regions found in all but the most distant interaction (largest  $R_P$ ) scenarios: a first burst that peaks for the closest encounters between  $10^6 - 10^7 M_{\odot} \text{ yr}^{-1}$  and lasts for 0.5 to 1 second centered at periapsis ( $t \sim 0$ ). This initial burst is followed by a quasi-static phase with magnitudes in the range  $10^2 - 10^4 M_{\odot} \text{ yr}^{-1}$  and a time dependence which, at least for the closest encounter cases, scales roughly as  $\dot{M} \propto 10^{-0.9t}$  as the flow begins to circulate around the black hole one to two seconds after periapsis. The range of accretion rates found in the quasi-static phase is considerably greater than the rate ( $\sim 50 M_{\odot} \text{ yr}^{-1}$ ) associated with background gas accretion represented by the horizontal line in Figure 6. The background accretion rate is highly sensitive to the background density set in the calculations, but the quasi-static rate is not and appears only to be affected by grid resolution which dictates coverage of the BH surface boundary and numerical dissipation. Comparing against purely hydrodynamic calculations, we find nuclear burning enhances mass accretion rates, total accreted mass, and peak density and temperature tracks by modest amounts, roughly 5-10%.

These accretion rates are many orders of magnitude greater than the rates expected from Eddington-limited accretion, which, assuming a standard 10% radiative efficiency, implies a rate

$$\dot{M}_{\text{Edd}} = \frac{L_{\text{Edd}}}{0.1c^2} = 4 \times 10^{-5} \left( \frac{M_{\text{BH}}}{10^3 M_{\odot}} \right) M_{\odot} \text{ yr}^{-1}, \quad (24)$$

for hydrogen-poor gas with electron scattering opacity  $\kappa_{\text{es}} = 0.2(1 + X_H) \rightarrow 0.2 \text{ cm}^2 \text{ g}^{-1}$ , where  $L_{\text{Edd}} = 4\pi cGM_{\text{BH}}/\kappa_{\text{es}}$ . Assuming a late-time fall-back scaling of  $t^{-5/3}$  (Rees 1988) applied at a return time of  $\approx 10^2$  s, we can reasonably expect these disruption events to emit x-ray and  $\gamma$ -ray transients and shine at Eddington luminosity for a year or more.

#### 4.2. Nucleosynthesis

One of the objectives of this work is to extend the results of RRH09 to the relativistic regime, and provide independent validation concerning the nucleosynthetics of TDEs using alternative high resolution grid-based numerical techniques and expanded nuclear reaction networks. RRH09 used SPH methods coupled with a 7-isotope  $\alpha$ -network to explore a multi-dimensional parameter space of TDEs covering a range of black hole masses, WD masses, and tidal strengths in search of conditions under which explosive nuclear burning can occur. They found a generically universal dependence on tidal strength and to a lesser degree on the WD mass. In particular they found ignition occurs when  $\beta \geq 3$  ( $\beta \geq 5$ ) for 1.2 (0.2 and 0.6) solar mass WDs. Their results also suggest a nominal dependence on the central potential model, generally finding stronger reactions (greater iron-group production) with a pseudo-potential that accounts for some near-field relativistic effects compared to purely Newtonian treatments. Hence our interest in exploring fully general relativistic interactions.



Additionally, recent studies by [Tanikawa et al. \(2017\)](#) have shed some doubt on the reliability (or limitation) of multi-dimensional numerical calculations due to the difficulty of allocating sufficient resources in the central ignition region. They argue coarse resolution does not adequately resolve shock heating and can produce spurious heating and artificially trigger ignition. At tidal strengths  $\beta \sim 5$ , [Tanikawa et al. \(2017\)](#) suggest a spatial resolution of about  $10^6$  cm is required to resolve the scale height sufficiently in order to produce reliable or convergent nuclear reactants. We have adapted our hybrid AMR/moving mesh technique to achieve slightly better than the recommended resolution ( $\lesssim 10^6$  cm) in the central orbit plane, improving on previous work by about an order of magnitude.

A number of diagnostics can be used to quantify the activation or efficiency of nuclear ignition, including calcium- and iron-group element production and the total amount of energy released from thermonuclear reactions. We discuss element production in subsequent paragraphs, but focus first on energy release. The total energy produced by nuclear reactions is presented in [Table 2](#) for all the cases we considered, and in [Figure 7](#) from a select sample. This quantity is not strongly sensitive to spatial resolution, and is thus a fairly robust measure of thermonuclear ignition. The trend for energy production is generally monotonically increasing with decreasing  $R_P$  (or increasing  $\beta$ ) as the WD experiences greater compression, so long as significant chunks are not captured by the BH to limit the amount of nuclear fuel available for production. This effect is observed comparing B3M2R09 and B3M2R06. The latter produces slightly less nuclear energy and iron elements despite achieving higher peak density and temperature.

We find all of our calculations ( $\beta \geq 2.6$ ) ignite, but only those cases with  $\beta \gtrsim 4.5$  release nuclear energies comparable to the star’s binding energies ( $1.3 \times 10^{49}$  and  $1.3 \times 10^{50}$  erg for the  $0.2$  and  $0.6M_\odot$  WD, respectively). These results are generally consistent with [Rosswog et al. \(2009\)](#), as are in select (or common) cases the magnitudes of released nuclear energy. For example, comparing case B3M2R20 to run 6 from RRH09 (with identical tidal strengths  $\beta = 5$ ), we find  $e_{\text{NUC}}$  agrees to within a factor of two. However, as we point out below, this level of agreement is not found in all diagnostics.

An exploding star which releases more energy than its binding energy may not necessarily produce copious amounts of iron elements. Hence we look separately at the mass of iron-group products as a complimentary measure of ignition efficiency. For the 19-isotope network used in our calculations, iron-group is defined as the sum of iron and nickel isotopes. The peak abundance of iron summed over the entire grid in each simulation is shown in [Table 2](#), and plotted as a function of time in [Figure 8](#) for a couple representative cases along with the other isotopic species. We additionally introduce silicon- (sum of Si, S and Ar) and calcium- (sum of Ca, Ti, and Cr) group elements to down-sample and simplify the number of species curves in [Figure 8](#). A comparison of the particular case B3M2R09 (left panel) can be made to [Figure 8](#) in RRH09 by further combining our silicon and calcium group curves. Although not identical, run 2 in RRH09 and B3M2R09 set the same WD and BH masses and comparable  $\beta$  (11 versus 12). We observe a similar mass deficit for helium elements, an iron abundance that agrees to within a factor of a few, but very different distributions of all the other minor isotopics. These differences might be explained by the adoption (or neglect) of trace elements in the initial data or simplifications necessitated by the different  $\alpha$ -chain networks (neither the 7 nor 19 isotope networks can be expected to accurately predict precise distributions, as each makes simplifications to the reality that would otherwise require modeling hundreds or perhaps thousands of isotopes and reaction paths). The right panel in [Figure 8](#) plots the species distributions for a moderately disrupted massive ( $0.6M_\odot$ ) WD, case B3M6R12. This is an interesting example where the nuclear flows are choked off before iron production can be completed. In this case, both calcium and silicon group elements dominate nickel and iron.

[Figure 9](#) plots a time sequence of three isosurface contours showing the distribution of helium, Ca-group, and Fe-group elements from the same case (B3M2R06) and times as [Figures 3](#) and [4](#). Ca-group elements are first formed when stellar matter is compressed to the proper density and temperature at and around periapsis, and preferentially along the inner surface closest to the black hole. Iron group elements are then subsequently formed in their (downstream) wake. Comparing the third time images in [Figures 3](#) and [9](#) shows nucleosynthesis is initiated where the star is maximally compressed along the dense radial filament cut across the star in the orbital plane as it passes periapsis. Nuclear products are then subsequently transported in a circular fashion and mixed alongside unignited stellar and background material around the black hole.

[Figures 10](#) and [11](#) present a different orthogonal view of the B3M6R06 event which highlights the complexity of reactive flows and demonstrates the need for high grid resolution. The left and right panels in [Figure 10](#) are taken at the same time ( $t = 0$ ) and represent the same quantities, but are calculated at different grid resolutions: the left panel at L2, the right at L3. In both images, red represents the mass fraction of combined carbon and oxygen (the initial composition for this event), and blue represents the combined mass fractions of nuclear products (Si+Ca+Fe groups).

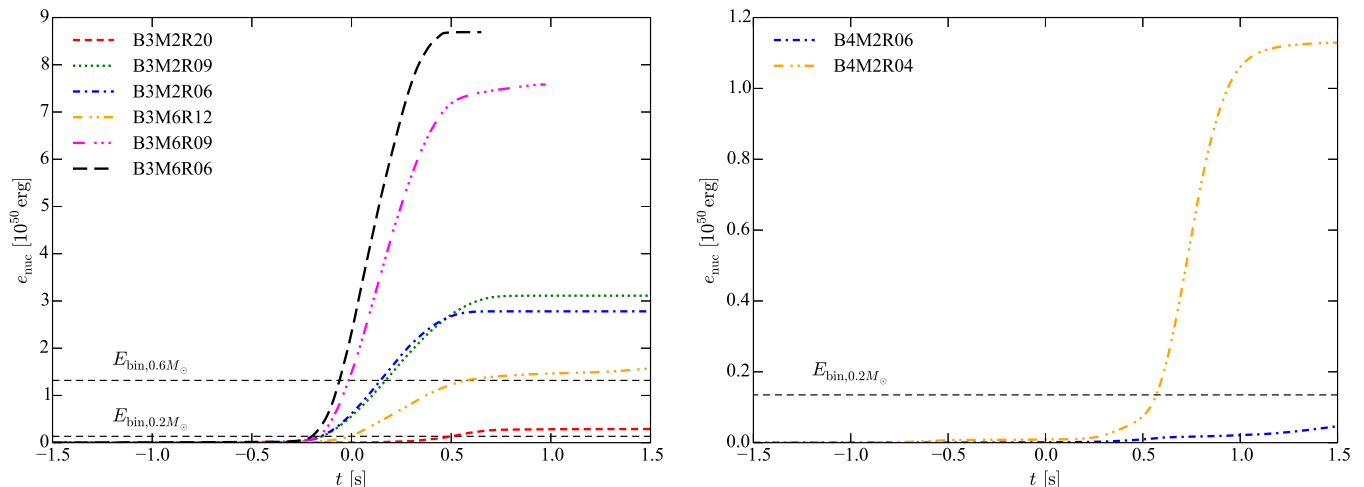


**Figure 7.** Nuclear energy generation for WD encounters with a  $10^3 M_\odot$  (left) and  $10^4 M_\odot$  (right) black hole.

Figure 11 shows the mass density (in color) and the velocity flow (aligned with the arrows) corresponding to the high resolution panel. In this orientation, the black hole is behind the (zoomed in) stellar matter which is moving from right to left around the black hole, as it pinches to maximum compression then bounces off the orbital plane. The dense radial filament observed in Figure 3 (though for a different case B3M2R06) is orthogonal to the image plane and projects towards the black hole at the point of maximum compression located approximately in the middle of these images (vertically and horizontally). The vertical scale of the image is zoomed in to roughly 6% of the initial star domain. The physical length scale between tick marks is the same in both vertical and horizontal axes. These images complement Figures 9, providing a more complete picture of the disruption process and begin to demonstrate the complex structure of the WD core when it ignites. As noted earlier, nuclear products first form at and along the pinched feature where density and temperature are highest, responding in time to the evolving shock structure off the orbital plane producing interpenetrating isotopic distributions, then transport downstream as they mix with other material.

The total mass of iron-group elements calculated by RRH09 for 0.2 (0.6)  $M_\odot$  WDs ranged anywhere from negligible up to 0.034 (0.0003)  $M_\odot$  for the BH masses we have considered, peaking at tidal strength  $\beta = 12$  with a 0.2  $M_\odot$  WD, and at  $\beta = 5$  with a 0.6  $M_\odot$  WD. Interestingly we find significantly greater iron-group production in our calculations: 0.089 (0.37)  $M_\odot$  for 0.2 (0.6)  $M_\odot$  WDs at  $\beta = 11$  (8.9). We thus observe three times greater iron production from 0.2  $M_\odot$  WDs, and at least an order of magnitude more from 0.6  $M_\odot$  WDs even after scaling down the tidal strength to the values quoted in RRH09.

We have additionally considered interactions with large periapsis radii and small to moderate  $\beta$  in order to explore the possibility of producing calcium-rich debris and evaluate whether tidal disruption events are viable sources of observed calcium-rich gap transients (Sell et al. 2015), despite the fact that many of these trajectories are further from the black hole and do not require full relativistic treatment. As Table 2 shows, we have systematically varied parameter sets to approach the low density regime that is most likely to produce conditions capable of prematurely terminating nuclear reactions and give rise to dominant calcium group elements (Ca, Ti, Cr) or IMEs rather than iron or nickel. Holcomb et al. (2013) calculated the smallest critical spatial scale  $\xi_{\text{crit}}$  that is required for helium detonation at these densities, finding  $\xi_{\text{crit}} \approx 10^9$  ( $10^7$ ) cm at  $\rho \approx 10^5$  ( $10^6$ ) g cm $^{-3}$ , well above our grid resolution. They argue incomplete burn occurs if the size of the fuel reservoir is comparable to  $\xi_{\text{crit}}$ , which it is at densities approaching  $10^5$  g cm $^{-3}$ . We find, as shown in Table 2, a direct correlation of systematically weaker reactions as this density is approached, but a regime clearly exists where Ca group elements dominate over iron and nickel production before nuclear ignition eventually fails at large  $R_p$ . Table 2 suggests that conditions which give rise to Ca-rich debris are not particularly efficient at nucleosynthesis. So although calcium-rich outflows can indeed be produced by tidal disruption with IMBHs at low interaction strengths  $\beta \lesssim 5$ , the resulting outflows, at least for the encounter parameters we have considered, will consist of  $\lesssim 0.03 M_\odot$  in the form of IMEs, converting roughly 14% of available fuel mass.

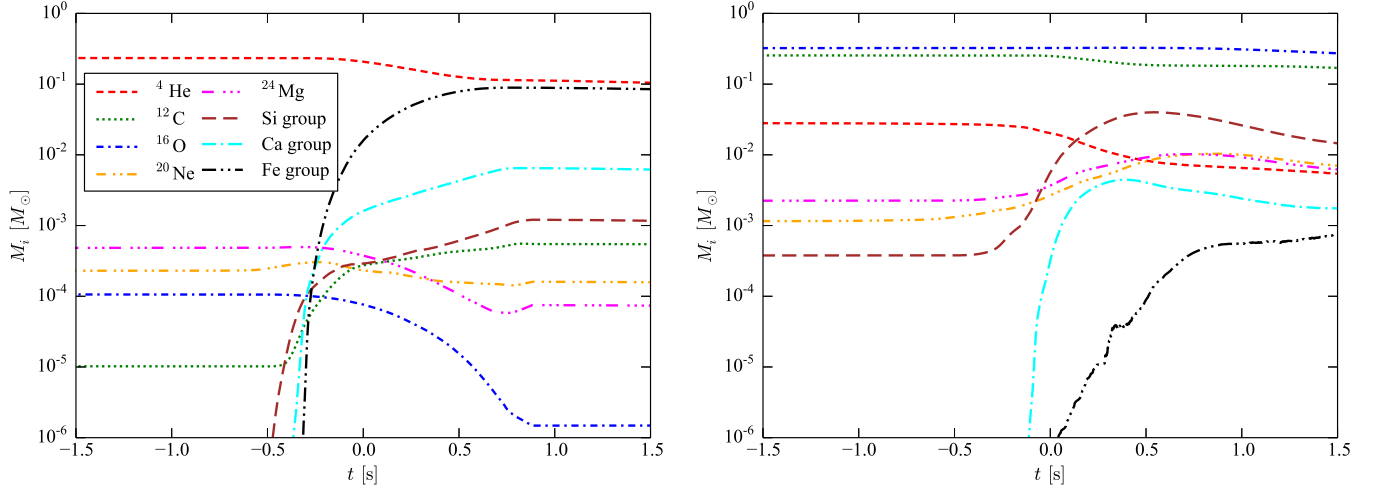


**Figure 8.** Nuclear species mass evolution for simulations B3M2R09 (left) and B3M6R12 (right). The legend is the same for both panels.

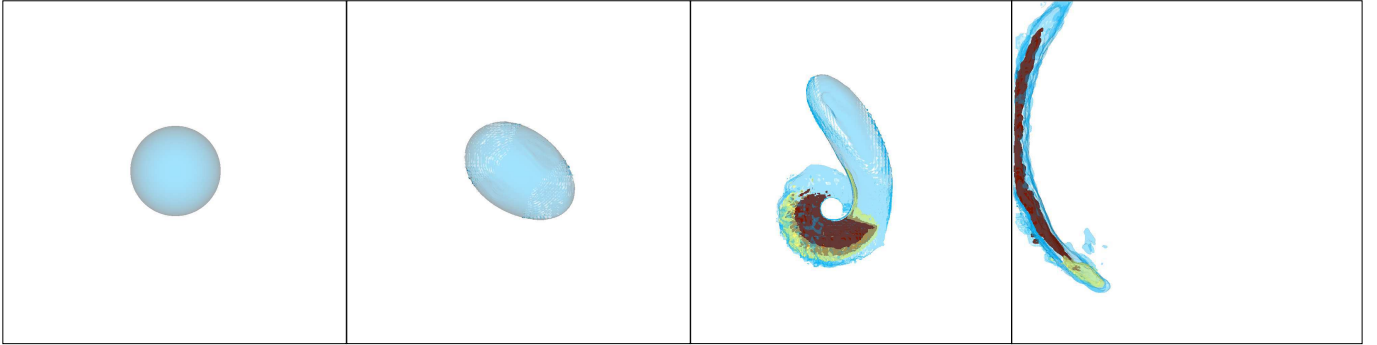


**Figure 9.** Isosurface plots indicating the distribution of helium ( $2000 \text{ g cm}^{-3}$ ; light blue), calcium-group ( $400 \text{ g cm}^{-3}$ ; pale yellow), and iron-group ( $7000 \text{ g cm}^{-3}$ ; burgundy) from the B3M2R06 run viewed from normal to the orbital  $x$ - $y$  plane at the same times as in Fig. 3.

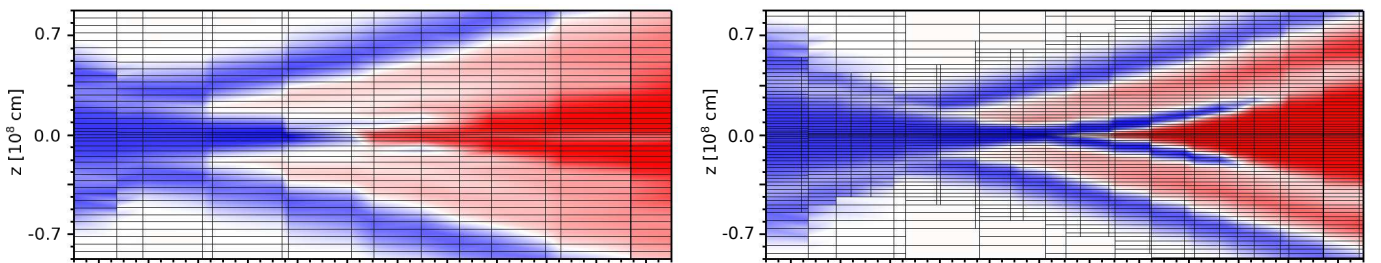


**Figure 10.** Cross section at  $t = 0.0 \text{ s}$  of the star centered on (and normal to) the overdense filamentary structure highlighted in the third plate of Figure 3. Red colors represent the abundance (mass fraction from 0 to 1) in  $^{12}\text{C}+^{16}\text{O}$ , while blue colors represent the abundance of nuclear reaction products (Si+Ca+Fe) from the B3M6R06-L2 (left) and B3M6R06 (right) runs. The grid mesh is included to depict how well resolved different features are.

In addition to distant encounters with  $10^3 M_{\odot}$  BHs, calcium-rich transients may also arise from close encounters with more massive  $10^4 M_{\odot}$  BHs. The range of tidal strengths accommodated by more massive BHs is severely restricted and consequently less energetic from a nucleosynthesis perspective. Stars cannot be initialized with periapsis radius closer than about four Schwarzschild radii, or tidal strengths greater than  $\beta \sim 5$ , without being promptly captured by the black hole (see Figure 2). This is a relatively weak interaction regime where we observe little nuclear activity,

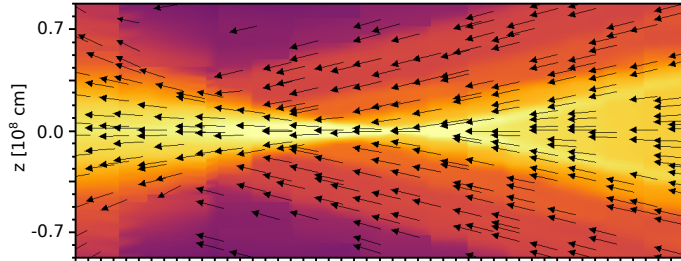


**Figure 11.** Same as right panel of Figure 10, except the velocity vectors are shown superimposed on the mass density. The density scale is the same as in Figure 3.

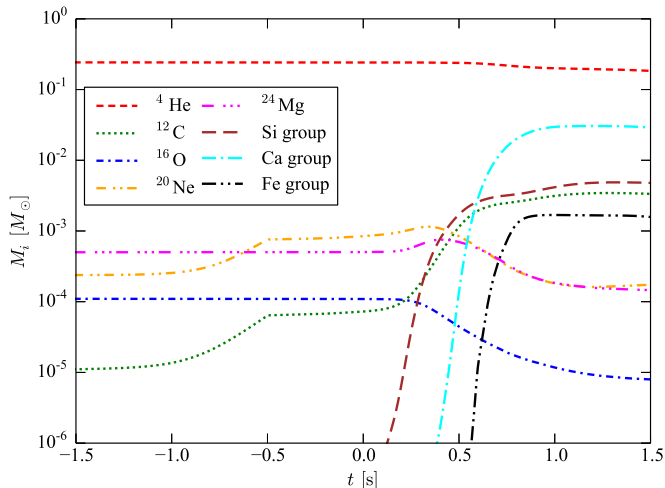


**Figure 12.** Nuclear species mass evolution for simulation B4M2R04.

so we limit the number of case studies involving  $10^4 M_\odot$  BHs to just two calculations. These two cases, however, prove to be excellent candidates for calcium-rich gap transients precisely because of their unique property of sampling both weak tidal strengths and ultra-close encounters. In fact, case B4M2R04 is an example of a moderate strength interaction ( $\beta = 5.4$ ) at the closest perihelion radius we have considered, and produces the greatest mass fraction of calcium-group elements in a calcium-rich environment as demonstrated in Figure 12. Figure 13 shows these transient candidates develop similar layered compositions as their iron-rich counterparts, except the dense inner core is composed of calcium-group elements, surrounded by smaller atomic mass elements (e.g., silicon).

#### 4.3. Post-processed Nucleosynthesis

Table 2 suggests that density-temperature phase tracks are fairly well converged at our highest resolution. We have therefore extracted time histories of density and temperature for the densest 10% of matter in the WD for a few cases, and run a much larger nuclear reaction network on that point-dimensional data to get a better picture of the full range of element synthesis in the dense WD core and to compare it against the smaller inline network results. The cases we have chosen for post-processing in this way include B3M2R06 and B3M6R06, the strongest reacting 0.2 and 0.6  $M_\odot$  WDs, respectively. Because we do not evolve the entire star, but only a sample of its dense core, we simplify the initial isotopic composition and set it to either pure helium or a 50% carbon/oxygen mixture for the 0.2 and 0.6  $M_\odot$  WDs, respectively. The data is evolved in time using the Torch code (Timmes 1999) to solve stand-alone 19 and 640 isotope reaction networks with time-dependent density and temperature track profiles as inputs, solving the network system to convergence over each discrete time interval before adjusting density and temperature for the next cycle. Of course these track histories don't necessarily correspond to contiguous fluid lines, but they are nonetheless useful for probing reactive transitions in the dense core.

The two cases (B3M6R06 and B3M2R06) are similar in that the 640 network converts more than 90% of nuclear fuel to iron-group elements, respectively 1.5 and 3 times greater percentage than the global fractions shown in Table

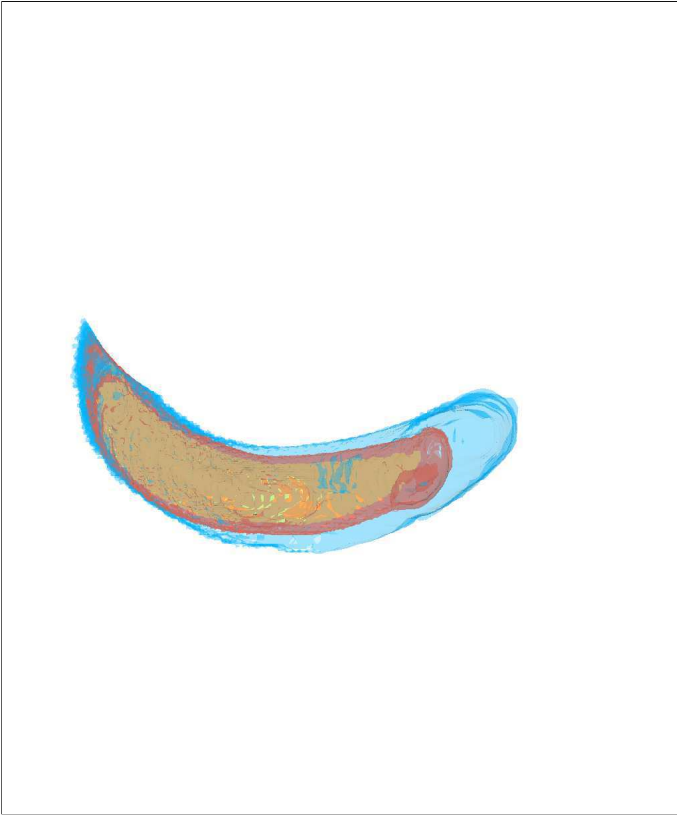


**Figure 13.** Isosurface plots indicating the distribution of helium ( $240 \text{ g cm}^{-3}$ ; light blue), silicon-group ( $1.2 \text{ g cm}^{-3}$ ; orange), and calcium-group ( $1.2 \text{ g cm}^{-3}$ ; pale yellow) from the B4M2R04 run viewed from normal to the orbital  $x$ - $y$  plane at time 1.0 sec.

2. Global fractions are understandably lower since they sample all stellar material at very different densities and temperatures beyond the core where iron elements predominately reside. This is supported by independently post-processing the dense core data using the same 19 isotope network adopted in the simulations. The 19 and 640 models predict roughly the same iron-group fraction, differing only by a few percent, giving greater confidence in the ability of the smaller network to provide reasonable predictions. Although the end product from the post-processing comes out almost entirely  $^{56}\text{Ni}$ , the 3D simulations predict 84% (B3M6R06) and 71% (B3M2R06) of iron-group elements are in the form of  $^{56}\text{Ni}$ , most likely attributed to the treatment of photodisintegration. At the high temperatures achieved in these ultra-close encounters, photodisintegration is very efficient. Burn products which form while the WD is undergoing initial compression are immediately disassembled when temperatures approach  $6 - 7 \times 10^9 \text{ K}$ . Iron-group elements do not form in substantial quantity until stellar material decompresses and cools to where alpha capture can proceed uninhibited. Although this effect is observed in some of the species plots from the 3D simulations, it is not as dramatic since that data represent globally integrated mass fractions and thus sample a range of temperatures at any single time. It is in these photo-processes where the small and large networks differ the most: The 19 species model tends to over-estimate photodisintegration and produce more stable iron isotopes at the expense of nickel. Hence the nickel fractions found in the 3D simulations and quoted above are likely a lower bound to what a larger network might predict.

Figures 14 and 15 compare production factors as a function of atomic mass from the 3D simulations (red symbols) against the 640-isotope Torch model applied to the dense core tracks (black symbols). All data points represent the final mass fractions in each run accounting for radioactive decay collapsing all species with a common mass number to their stable form. These are then normalized to the mass fraction in the sun of the stable species. Connecting lines indicate isotopes of a given element (listed in the figures), a star indicates the most abundant isotope of a given element. Circles represent isotopes that were made as themselves, while triangles indicate that the stable species was made as a radioactive progenitor. As reactions proceed along the proton-rich side of the alpha chain, they produce



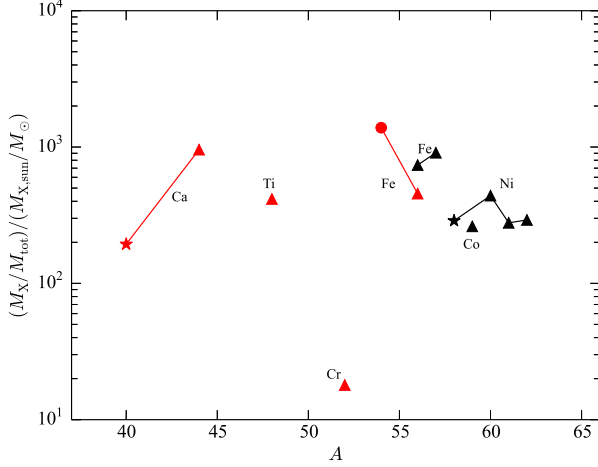


**Figure 14.** Production factor of nuclei produced in the 3D simulation of B3M6R06 (red) and post-processed dense core tracks (black). Species connected by solid lines are isotopes of the same element (shown), species indicated by a circle are made as themselves, species indicated by a triangle are made radioactively (and decay to the element shown), species indicated with a star represent those made as themselves that also have the largest mass fractions in nature.

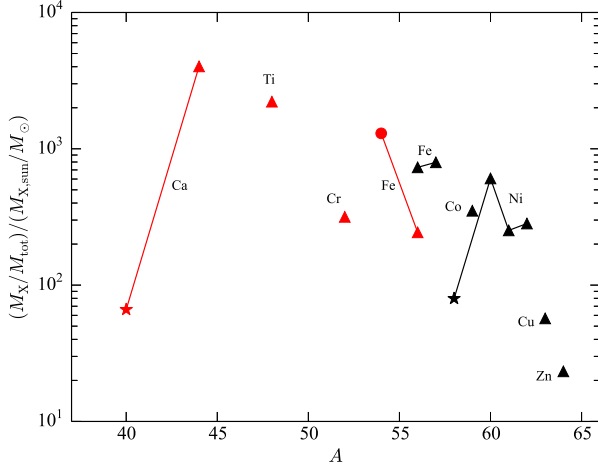


**Figure 15.** As Figure 14 but for case B3M2R06.

stable nuclei up to  $^{40}\text{Ca}$ , after which unstable nuclei are formed beginning with  $^{44}\text{Ti}$  and produced in our calculations at very high relative (to solar) abundance as indicated in both figures. Notice that although calcium represents a small fraction of elements produced in the 3D simulations, it is comparable to iron and nickel when normalized by solar abundance. Notice also the extracted phase track results (represented by black symbols) come out almost entirely as iron-group elements and cannot properly predict the creation of IMEs forming outside the WD core since they sample only the densest parts of the WD. This point was made in a previous paragraph, but emphasized nicely in both Figures 14 and 15. In general the post-processed results suggest conditions similar to Type 1a supernovae and to incomplete silicon burning and nuclear statistical equilibrium in Type 2 supernovae: the dominant species produced are  $^{56}\text{Fe}$  and  $^{57}\text{Fe}$  made as radioactive nickel, both of which have been observed through  $\gamma$ -line emission in SN1a and SNI. Yet heavier species of cobalt and nickel (made as copper and zinc) are co-produced, but the interesting species  $^{64}\text{Zn}$  (made as  $^{64}\text{Ge}$ ) is not made in amounts that would suggest tidally disrupted WD's as a possible production site.

Though many details are lost with the 19-isotope model adopted in this work, this exercise demonstrates, among other things, that it is a fairly good approximation to the overall solution and accurately predicts the dominant end

products. But it is also clear that significant nuclear reactions take place outside the dense WD core where IMEs are most likely to reside, and that a more accurate post-processing treatment will require fluid tracers to resolve nucleosynthesis on a global scale across the entire WD.

#### 4.4. Gravitational Waves

Tidal disruption events are potential sources of strong gravitational waves, particularly during the early phase when the star is sufficiently compact and the interaction highly asymmetric. After passing periapsis, however, the resulting tidal forces disrupt the star into an extended debris tail and the wave signal diminishes significantly. Gravitational wave emissions from TDEs will therefore have burst-like behavior with estimated amplitude (RRH09)

$$h \approx \frac{GM_{\text{WD}}R_{\text{S}}}{c^2 R_{\text{P}} D} \approx 1 \times 10^{-22} \beta \left( \frac{D}{10 \text{ Mpc}} \right)^{-1} \left( \frac{M_{\text{WD}}}{0.6 M_{\odot}} \right)^{4/3} \left( \frac{R_{\text{WD}}}{10^9 \text{ cm}} \right)^{-1} \left( \frac{M_{\text{BH}}}{10^3 M_{\odot}} \right)^{2/3}, \quad (25)$$

and frequency

$$f \approx \left( \frac{GM_{\text{BH}}}{R_{\text{P}}^3} \right)^{1/2} \approx 0.1 \beta^{3/2} \left( \frac{M_{\text{WD}}}{0.6 M_{\odot}} \right)^{1/2} \left( \frac{R_{\text{WD}}}{10^9 \text{ cm}} \right)^{-3/2} \text{ Hz}, \quad (26)$$

placing the encounter scenarios we have considered within the anticipated frequency range of LISA (Amaro-Seoane et al. 2017).

More precisely, we calculate the retarded wave amplitudes of both polarizations,  $h_+$  and  $h_{\times}$ , for an observer along the  $z$ -axis at distance  $D$  from the source using the quadrupole approximation

$$Dh_+ = \frac{G}{c^4} (\ddot{I}_{xx} - \ddot{I}_{yy}), \quad (27)$$

$$Dh_{\times} = \frac{2G}{c^4} \ddot{I}_{xy}, \quad (28)$$

where  $\ddot{I}_{ij}$  is the second time derivative of the reduced quadrupole moment of the mass distribution. In practice, the second time derivatives are eliminated through substitution of the hydrodynamic evolution equations and integration by parts, to produce an expression easily calculated from evolved fields (Camarda et al. 2009). We plot in Figure 16 a sample of computed waveforms that showcase their diversity with different WD and BH mass and interaction combinations. Figure 17 plots the strain amplitude (assuming a 10 Mpc source distance) and frequency for most of our simulations. The strain amplitude is computed as  $\sqrt{h_+^2 + h_{\times}^2}$ , while the frequency is defined simply as the inverse of twice the time interval between the first minimum and first maximum in the  $h_{\times}$  signal. The solid lines in Figure 17 represent the estimated dependencies predicted by equations (25) and (26). We find that the  $\beta^1$  and  $\beta^{3/2}$  analytic scalings for the amplitude and frequency, respectively, are, to within small normalization factors, well represented by the data at sufficiently small  $\beta$ , but deviate significantly at large tidal strengths ( $\beta > 10$ ). Although our parameter space does not sample black hole or white dwarf masses sufficiently to verify their analytic scalings (we considered only two values for each), we do note that both strain and frequency scalings are generally consistent with predictions, increasing with both  $M_{\text{WD}}$  and  $M_{\text{BH}}$ . We also note that the addition of nuclear burning does not significantly affect wave signals. We find, for instance, wave amplitudes with and without active nucleosynthesis match to within a fraction of a percent.

Gravitational wave attributes for all events we considered are packed tightly between strain amplitudes  $0.5 \times 10^{-22}$  -  $3.5 \times 10^{-22}$  at 10 Mpc source distance, and frequencies 0.1 - 0.7 Hz, just below and outside the frequency range of LIGO (Abbott et al. 2016). Although these signals fall within LISA's frequency band, the amplitudes are sufficiently small that they will not likely be observed except at source distances within 10-100 kpc, which, if current estimates of the WD-IMBH disruption rate ( $500 \text{ yr}^{-1} \text{ Gpc}^{-3}$ ) are correct, would be extremely rare events.

## 5. CONCLUSIONS

We have developed a novel numerical methodology based on a combination of moving mesh and adaptive mesh refinement, and applied it to simulate the tidal disruption of white dwarf stars from near encounters with non-rotating, intermediate mass black holes. We solve the general relativistic hydrodynamics equations in a Kerr-Schild background spacetime, to account for relativistic tidal forces. The AMR/moving mesh hybrid approach allows us to move the base grid along Lagrangian fluid lines, while at the same time refining on the densest parts of the white dwarf as it

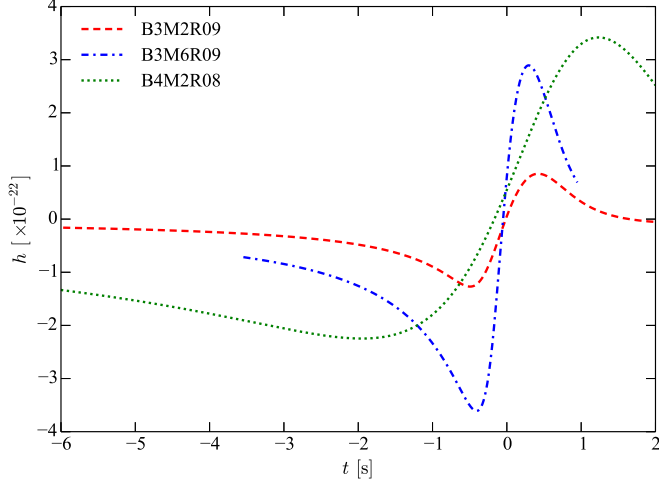


**Figure 16.** Gravitational wave forms ( $h_{\times}$  polarization) for a sampling of simulations with different WD and BH masses, each assuming a source distance of  $D = 10$  Mpc.

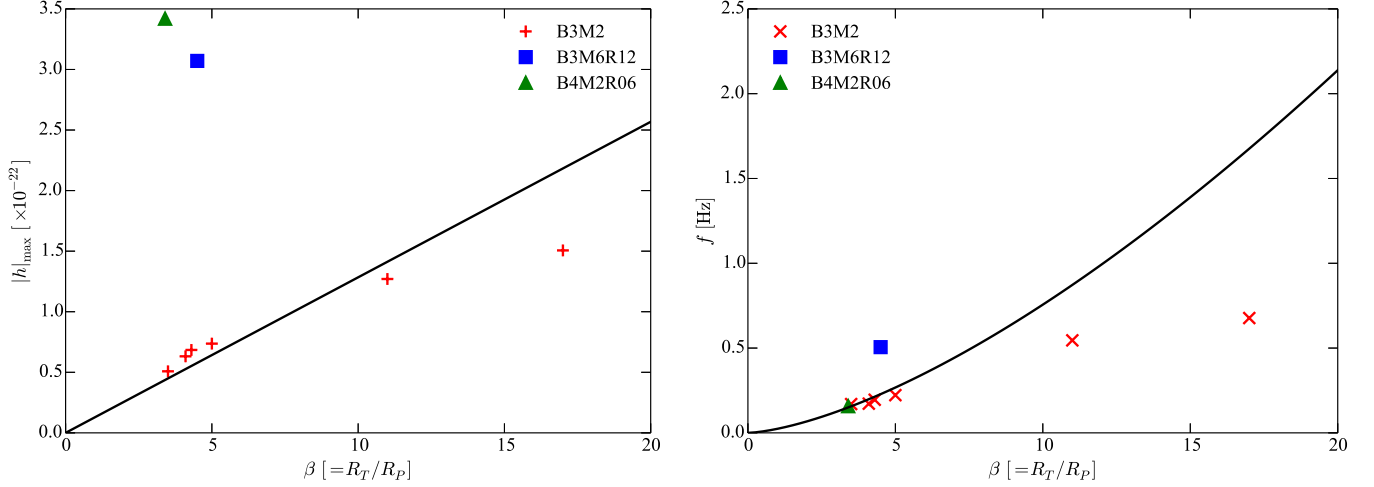


**Figure 17.** Gravitational wave amplitude (at 10 Mpc source distance, left) and frequency (right) as a function of  $\beta$ . The predicted scalings from equations (25) and (26) (solid lines) apply to the B3M2 family of simulations, while the other points are included to demonstrate proper scalings with  $M_{\text{WD}}$  and  $M_{\text{BH}}$ .

compresses and stretches from tidal forces. This is critical in order to achieve sufficient zone resources in the central plane regions and provide the necessary scale height coverage to resolve internal shock and ignition features, which in turn are critical to approach convergent nuclear reactive solutions. A comprehensive study by [Tanikawa et al. \(2017\)](#) suggests a resolution of  $\leq 10^6$  cm is needed to properly resolve nuclear flows for moderate tidal strength interactions ( $\beta \approx 5$ ). Previous three dimensional calculations, (e.g. RRH09, HSBL12) fell short of that standard by about an order of magnitude. The calculations presented here, to our knowledge, thus represent the highest resolution 3D studies of these systems to date, achieving vertical resolution of slightly better than  $10^6$  cm. However, we caution that even this resolution is almost certainly inadequate at high interaction strengths.

In addition to improved spatial resolution, this work expands on previous investigations by accounting for general relativistic hydrodynamics coupled with nuclear reactions composed of a larger isotopic network and more accurate energy production estimates. The combination of high resolution and inline nuclear reactions makes these calculations computationally expensive. Nuclear reactions by themselves increase run times by about a factor of a few compared to pure hydrodynamics, depending on local state conditions and reactive response times. As a consequence

our calculations are terminated between one to two seconds after the white dwarfs pass periapsis along parabolic trajectories. However, this is more than enough time for nucleosynthesis to complete at 1% relative energy production levels ( $\delta e_{\text{nuc}}/(e \delta t) < 0.01$ ).

Our choice of parameters is motivated by a desire to sample WD mass, BH mass, and periapsis radius to elucidate the effects of relativity, compression ratios, and thermodynamic response on nuclear reactions. Options for a 0.2 or 0.6  $M_{\odot}$  WD brings in different initial hydrodynamic conditions (density, pressure, temperature), but also different isotopic compositions (predominately either helium or a carbon-oxygen mixture initializing isotopic mass fractions with trace amounts of minor isotopics). BH mass of  $10^3$  or  $10^4 M_{\odot}$  affects tidal compression, elongation, and crossing/compression timescales. The periapsis radius modulates relativistic effects and proximity to the BH. Collectively, these combinations define a tidal strength parameter  $\beta = R_T/R_P$  (ratio of tidal to perihelion radii) which is critically important for predicting conditions necessary for nuclear ignition.

We find all of our calculations ignite, even at tidal strengths as low as  $\beta = 2.6$ , creating a wide variety of environments capable of converting tidal debris into arbitrary combinations of intermediate and high mass elements (or mass ratio of burn products) simply by adjusting the tidal strength parameter. In a crude sense, considering the debris is far from spherical, stellar matter assembles into compositions resembling SN Ia models in that the densest parts are composed mostly of iron-group elements (or otherwise heaviest possible nuclei depending on the interaction strength), surrounded by IMEs and an outer layer of unburned fuel. Stronger interactions (greater  $\beta$ ) of course give rise to systematically greater energy release and nuclear production of iron group elements. At tidal strengths  $\beta \gtrsim 4.5$  the amount of released nuclear energy exceeds the binding energy of the stars. This result is consistent with RRH09, as are predictions of the released energy (to about a factor of two) when we compare runs with comparable interaction strengths. However, our calculations tend to produce significantly greater amounts of iron group elements, with differences ranging from factors of three to orders of magnitude. A peak conversion efficiency, defined by the ratio of iron-group products to the initial stellar mass, of about 60% is observed in our closest encounter scenarios, most of which is in the form of  $^{56}\text{Ni}$ .

These differences are not surprising considering the sensitivity of element production to spatial resolution, the strong dependence of reaction rates on temperature and therefore the equation of state, and the limitations of small  $\alpha$ -chain networks to calculate heavy element production. It is unclear how much of the observed differences from previous work is due to improvements made in this paper (general relativity, increased grid resolution, and extended network model), to different initial stellar conditions (density, temperature, isotopic distributions), or to the approximation made for the equation of state and therefore the temperature that is critical for nucleosynthesis. Any combination of these possibilities could contribute to the factor of two differences observed in the total energy production diagnostic. However the much greater differences in iron-group production are not as easily explained and requires further study.

We have additionally investigated whether tidally disrupted WDs might be viable sources of observed calcium-rich gap transients (Sell et al. 2015). These gap transient systems are characterized by relatively large calcium abundances compared to iron or nickel, by factors of ten or more, and are thus representative of incomplete burning environments generally incapable of sustaining chain reactions through to iron-group production. Idealized one-dimensional calculations performed by Holcomb et al. (2013) suggest these regimes do exist and might be within the realm of conditions produced by tidal disruption events, particularly for low mass white dwarfs at densities between  $10^5$  and  $10^6 \text{ g cm}^{-3}$  and temperatures  $\sim 10^9 \text{ K}$ . Kawana et al. (2017) in their investigations did not observe calcium-rich products, but noted densities found in their calculations were slightly higher than  $10^6 \text{ g cm}^{-3}$ . We point out that conditions appropriate for producing Ca-rich transients are achieved through moderate to weak tidal interactions,  $\beta \lesssim 5$ , where scale height resolution requirements are less demanding and marginally resolved with current methods. Our investigations show Ca-group elements do dominate over iron and nickel masses at tidal strengths producing relatively low density cores, with a clear trend for increasing calcium to iron abundance ratio with decreasing  $\beta$ . However, we also find nuclear reactions at these conditions are inefficient, converting less than 15% of available fuel to burn products, the precise composition of which is a strong function of tidal strength. So, although we have demonstrated that Ca-rich debris can be produced from the tidal disruption of WDs by IMBHs, the associated cooler, low density environments produce corresponding outflows with limited amounts of IMEs ( $\lesssim 0.03 M_{\odot}$ ).

Mass accretion rates are strongly dependent on the interaction strength and proximity to the BH, but invariably well above Eddington-limited rates. We can reasonably expect these interactions to emit x-ray and  $\gamma$ -ray transients and shine at Eddington luminosity for more than a year. Rates are generally characterized by a large prompt burst (for sufficiently close  $R_P \lesssim 12$  encounters) lasting between 0.5 to 1 second during periapsis approach, followed by

a quasi-static phase with a shallower decay profile that scales roughly as  $\dot{M} \propto 10^{-0.9t}$  during the onset of the circularization phase. At larger perihelion radius, the prompt accretion rate is weak, so the quasi-static phase is the only distinguishable feature of distant encounters. The amplitude of the prompt burst is strongly influenced by tidal strength, and peaks between  $10^6 - 10^7 M_\odot \text{ yr}^{-1}$  for ultra-close encounters. Quasi-static accretion rates do not vary as much with tidal strength and are typically confined to a much smaller and narrower range  $10^2 - 10^4 M_\odot \text{ yr}^{-1}$  at  $R_P \lesssim 12$ . We find nuclear burning enhances the mass accretion rate, but only by a modest 10%.

Finally, the encounter scenarios considered here generate burst-like gravitational waves with amplitudes that are not sensitive to nuclear burning, and that scale nonlinearly with tidal strength and vary between  $0.5 \times 10^{-22} - 3.5 \times 10^{-22}$  at 10 Mpc source distance. Their characteristic frequencies fall in the range 0.1 - 0.7 Hz, just below LIGO's frequency band but potentially observable with LISA for admittedly rare events at source distances within 10-100 kpc.

This work was performed in part under the auspices of the U.S. Department of Energy by Lawrence Livermore National Laboratory under Contract DE-AC52-07NA27344. It used resources from the Extreme Science and Engineering Discovery Environment (XSEDE), which is supported by National Science Foundation grant number ACI-1053575. P.C.F. and B.M. acknowledge support from National Science Foundation grants AST 1616185 and PHY17-48958. B.M. also acknowledges support from NASA Astrophysics Theory Program grants NNX16AI40G and NNX17AK55G and NCN grant 2013/08/A/ST9/00795.

*Software:* Cosmos++ (Anninos et al. 2005, 2012, 2017), MESA (Paxton et al. 2011), Torch (Timmes 1999)

## REFERENCES

- Abbott, B. P., Abbott, R., Abbott, T. D., et al. 2016, *Living Reviews in Relativity*, 19, 1
- Amaro-Seoane, P., Audley, H., Babak, S., et al. 2017, *ArXiv e-prints*, arXiv:1702.00786
- Anninos, P., Bryant, C., Fragile, P. C., et al. 2017, *ApJS*, 231, 17
- Anninos, P., Fragile, P. C., & Salmonson, J. D. 2005, *ApJ*, 635, 723
- Anninos, P., Fragile, P. C., Wilson, J., & Murray, S. D. 2012, *ApJ*, 759, 132
- Baumgardt, H., Makino, J., & Ebisuzaki, T. 2004, *ApJ*, 613, 1143
- Brassart, M., & Luminet, J.-P. 2008, *A&A*, 481, 259
- Camarda, K. D., Anninos, P., Fragile, P. C., & Font, J. A. 2009, *ApJ*, 707, 1610
- Dong, X., Wang, T., Yuan, W., et al. 2007, *ApJ*, 657, 700
- Fragile, P. C., Gillespie, A., Monahan, T., Rodriguez, M., & Anninos, P. 2012, *ApJS*, 201, 9
- Fragile, P. C., Olejar, A., & Anninos, P. 2014, *ApJ*, 796, 22
- Gebhardt, K., Rich, R. M., & Ho, L. C. 2002, *ApJL*, 578, L41
- . 2005, *ApJ*, 634, 1093
- Gerssen, J., van der Marel, R. P., Gebhardt, K., et al. 2002, *AJ*, 124, 3270
- . 2003, *AJ*, 125, 376
- Guillochon, J., & McCourt, M. 2017, *ApJL*, 834, L19
- Haas, R., Shcherbakov, R. V., Bode, T., & Laguna, P. 2012, *ApJ*, 749, 117
- Holcomb, C., Guillochon, J., De Colle, F., & Ramirez-Ruiz, E. 2013, *ApJ*, 771, 14
- Kasliwal, M. M., Kulkarni, S. R., Gal-Yam, A., et al. 2012, *ApJ*, 755, 161
- Kawana, K., Tanikawa, A., & Yoshida, N. 2017, *ArXiv e-prints*, arXiv:1705.05526
- Khokhlov, A. M., & Ergma, E. V. 1986, *Soviet Astronomy Letters*, 12, 152
- Kobayashi, S., Laguna, P., Phinney, E. S., & Mészáros, P. 2004, *ApJ*, 615, 855
- Laguna, P., Miller, W. A., Zurek, W. H., & Davies, M. B. 1993, *ApJL*, 410, L83
- Lee, W. H., Ramirez-Ruiz, E., & Page, D. 2005, *ApJ*, 632, 421
- Luminet, J.-P., & Carter, B. 1986, *ApJS*, 61, 219
- Luminet, J.-P., & Pichon, B. 1989, *A&A*, 209, 103
- MacLeod, M., Guillochon, J., Ramirez-Ruiz, E., Kasen, D., & Rosswog, S. 2016, *ApJ*, 819, 3
- Paxton, B., Bildsten, L., Dotter, A., et al. 2011, *ApJS*, 192, 3
- Rees, M. J. 1988, *Nature*, 333, 523
- Reid, I. N. 2005, *ARA&A*, 43, 247
- Rosswog, S., Ramirez-Ruiz, E., & Hix, W. R. 2009, *ApJ*, 695, 404
- Sell, P. H., Maccarone, T. J., Kotak, R., Knigge, C., & Sand, D. J. 2015, *MNRAS*, 450, 4198
- Shcherbakov, R. V., Pe'er, A., Reynolds, C. S., et al. 2013, *ApJ*, 769, 85



Tanikawa, A., Sato, Y., Nomoto, K., et al. 2017, ApJ, 839,  
81  
Timmes, F. X. 1999, ApJS, 124, 241  
Timmes, F. X., Hoffman, R. D., & Woosley, S. E. 2000,  
ApJS, 129, 377

Weaver, T. A., Zimmerman, G. B., & Woosley, S. E. 1978,  
ApJ, 225, 1021